Research papers

Impacts of future land cover and climate changes on runoff in the mostly afforested river basin in North China

Wenting Yang[a], Di Long[a,*], Peng Bai[b]

[a] State Key Laboratory of Hydroscience and Engineering, Department of Hydraulic Engineering, Tsinghua University, Beijing 100084, China
[b] Key Laboratory of Water Cycle and Related Land Surface Processes, Institute of Geographic Sciences and Natural Resources Research, Chinese Academy of Sciences, Beijing 100101, China

ARTICLE INFO

ABSTRACT

The Luanhe River basin, the mostly afforested river basin in North China, has exhibited significant land use/land cover change (LUCC) under climate change that could jointly affect water availability of the basin in the future. This study examines both impacts of LUCC and climate change on runoff over the upper reaches of the Luanhe River basin. First, the land use in 2020 is predicted based on the Cellular Automata-Markov (CA-Markov). Second, a hydrological model (Soil Water Assessment Tools, SWAT) is set up for the baseline period 1961–1979 and driven primarily by outputs from five general circulation models (GCMs) under four representative concentration pathways (RCPs) (i.e., RCP2.6, RCP4.5, RCP6.0 and RCP8.5) for the period 2020–2030. Results show that the ensemble mean annual precipitation may increase under four RCPs for the period 2020–2030, with the maximum (470 mm/yr) and minimum (444 mm/yr) for RCP8.5 and RCP6.0, respectively, 1–7% higher than the observed mean annual precipitation (441 mm/yr) during 1961–1979. The relationship between the runoff simulations and the RCPs under the 2020 land use scenario is nonlinear, with the maximum (57 mm/yr) and minimum (50 mm/yr) mean annual runoff depths under the RCP4.5 and RCP6.0 scenarios, respectively, ~58% and ~39% higher than the mean annual observed runoff depth (36 mm/yr) for the baseline period. The increase in forestland (~56%) and decrease in agriculture land (~ −30%) are remarkable for the period 1970–2020, driven primarily by afforestation implemented in the Luanhe River basin. LUCC would lead to a slight decrease in mean annual runoff, and the runoff only increases in summer but decreases in other three seasons. The decrease in surface runoff and groundwater discharge jointly results in the overall decrease in runoff due to LUCC. In general, the climate change impact will dominate runoff change for the study basin, though marked afforestation has taken place and is likely to continue in the future.

1. Introduction

With the development of society and economy, various human activities have profoundly affected the hydrological cycle and water resources through different pathways (Li et al., 2007), and an important indicator of such impacts is the land use and land cover change (LUCC) (Deng et al., 2015; Lambin and Meyfroidt, 2011). LUCC has significant impacts on hydrological processes, as well as the economy and ecology of watersheds by regulating runoff generation and routing, and evapotranspiration (ET) (DeFries and Eshleman, 2004; Deng et al., 2003). The Luanhe River basin in North China features marked afforestation over its upper reaches since 1999 for the purposes of reducing sandstorm from Inner Mongolia to Beijing and soil and water conservation. Three large tree farms, i.e., Yudaokou, Qiansongba and Saibei were built during these years where the forest coverage rate reached almost

50% by 2016, and is expected to increase to 73% by 2021 (Li et al., 2017). There are two reservoirs in the midstream of the Luanhe River (i.e., the Panjiakou Reservoir and the Daheiting Reservoir), which are the most important surface water sources for Tianjin Municipality and Tangshan City (Cao et al., 2010; Li and Huang, 2015). The water division project from the Luanhe River to Tianjin increases water supply and improves water quality, and effectively reduces groundwater abstraction and land subsidence in Tianjin. Since the 1950s, the hydrological cycle in the Luanhe River basin has been remarkably changed, driven primarily by the combined effects of climate change and human activities (Liu et al., 2013). Due to less rainfall and the effect of soil and water conservation, decreases in mean annual runoff have been shown to reach 30% during 1980–2002, compared with the period 1956–1979, which may result in water supply crisis (Li et al., 2014). It is therefore imperative to predict changes in water availability by

---

* Corresponding author.
  E-mail address: dlong@tsinghua.edu.cn (D. Long).

considering both LUCC and climate change in the future, so as to formulate adaptation strategies to achieve sustainable use and allocation of water resources. Precipitation and streamflow in the Luanhe River basin have changed markedly after 1979 (Chen et al., 2013), so we selected the period 1961–1979 as the baseline period when both climate change and human activities had little effect on the basin. We predicted the land use map of 2020 using the land use transition matrix from 2000 to 2010, which is representative to show the LUCC due to afforestation. The corresponding future period 2020–2030 was selected to perform runoff simulation under the 2020 land use scenario, and the simulations were compared to the results for the baseline period.

Numerous studies have shown the impacts of LUCC on streamflow. Wei et al. (2007) classified 131 rainfall events into three regimes to analyze the runoff and soil loss in relation to different land use types. Runoff simulations under prescribed land use scenarios indicated that runoff increased when the grassland area increased and forestland decreased (Wang et al., 2008). Kathumo et al. (2011) found a strong relationship between streamflow and land use/land cover with a coefficient of determination (R^2) of 0.84 in the River Gucha catchment, Kenya. Dixon and Earls (2012) used the Soil and Water Assessment Tool (SWAT) to examine the effects of urbanization on streamflow. Simulations also showed that land use change can result in changes in surface runoff and groundwater recharge (Baker and Miller, 2013). Shi et al. (2014) analyzed the responsive relationship between the surface runoff variation and the major landscapes, suggesting that the conversion from forestland to farmland and grassland resulted in increases in mean annual surface runoff and total runoff. These results show that runoff can be an effective indicator of LUCC in watersheds (Bewket and Sterk, 2005).

Because of complicated driving factors and significant variations in LUCC (Li et al., 2010), it is challenging to predict LUCC precisely given the changing economy, land use policy, and natural variables (Iacono et al., 2012; Li and Huang, 2015). Previous studies used various approaches to depict LUCC, considering economic growth, population, social policies, and mutual feedbacks among them. A dynamic system was set up to model LUCC using different driving forces (e.g., land use management and population growth), and the future LUCC was simulated under different socio-economic policies, providing reference for decision making for sustainable development (Yu et al., 2011). The Markov chain model is a simple probabilistic land use change model based on the Markov process. In the process the current state depends only on its most adjacent previous period, and the transition can be described by transition probability matrices (Iacono et al., 2012). A Cellular Automata-Markov (CA-Markov) model was used to simulate forest cover changes of a national park to evaluate pre and post policy interventions, indicating positive effects of national level policy (Adhikari and Southworth, 2012). Changes in the relationships between precipitation and streamflow can also be indicative of LUCC (Gupta et al., 2015).

Runoff changes reflect the compound effects of LUCC and climate change. Some previous studies used the Coupled Model Intercomparison Project phase 5 (CMIP5) data set to analyze the impacts of climate change under different scenarios (Eisner et al., 2017; Eum et al., 2016; Neupane et al., 2015; Teklesadik et al., 2017). Results of the coupled climate model HadGEM2-AO reveal increases in precipitation over tropical regions but decreases over subtropical regions, given the expansion of Hadley cell over the 21st century. In addition, changes in soil moisture and sea ice under different representative concentration pathways (RCPs) also show spatial variability (Baek et al., 2013). Extreme precipitation events were evaluated over the Columbia River basin during 1970–1999 and 2041–2070 under the RCP8.5 scenario by simulating four CMIP5 general circulation model (GCMs) (Dars, 2013). Though the mean precipitation is projected to

decrease, the extreme precipitation events show significant increases in some regions. In addition, investigation into runoff extremes in the future has been done at a finer resolution than GCMs over the Pacific Northwest, using regional climate models projections (Najafi and Moradkhani, 2015). Moreover, some studies evaluated the impacts of climate change on streamflow to formulate water management strategies (Basheer et al., 2015; Ouyang et al., 2015). Previous studies have examined the accuracy of some outputs of GCMs in China (Chen and Frauenfeld, 2014; Chen et al., 2014; Sun et al., 2016), and there is a consensus that the resolution of the raw output of GCMs is too coarse to describe hydrological processes at regional scales (Dars, 2013; Ouyang et al., 2015; Wilby, 2004; Wilby et al., 1999; Ahmadalipour et al., 2017).

A number of studies have evaluated the impacts of climate change on runoff using multiple GCMs and hydrological models (Eisner et al., 2017; Teklesadik et al., 2017). However, climate modeling factors can also influence the variance of streamflow. Experiments using varied factors (e.g., GCM type, project phase, emission scenario, downscaling method, and bias correction) indicated that the predicted streamflow is a function of modeling factors, and it is unnecessary to consider all the factors as long as the ensemble design is well balanced (Aamery et al., 2016). Future impacts of LUCC and climate change on runoff can be evaluated simultaneously. In the Brahmaputra River basin, sensitivities of ET, streamflow, total water yield, groundwater recharge to CO_2 concentration, temperature, and precipitation changes were evaluated, indicating that ET and groundwater recharge are more sensitive to changes in CO_2 concentration and precipitation, respectively (Pervez and Henebry, 2015). More studies focusing on LUCC and climate change or their impacts on streamflow can be found in Table 1.

The overall objective of this study is to systematically investigate both impacts of LUCC (i.e., mainly afforestation) and climate change (i.e., mainly variations in precipitation) on future runoff for the upper reaches of the Luanhe River (i.e., the upper Panjiakou Reservoir). This objective of this study was achieved by performing these following four steps: (1) runoff simulation for the baseline period 1961–1979 under the 1970 land use scenario using SWAT; (2) prediction of the land use/ land cover in 2020 using CA-Markov; (3) runoff simulation for the period 2020–2030 under different land use/land cover scenarios (1970 and 2020) and four RCPs (i.e., RCP2.6, RCP4.5, RCP6.0, and RCP8.5); and (4) examination of both impacts of LUCC and climate change scenarios on future runoff (2020–2030). Results of this study should improve our understanding of variations in runoff for the study basin under a range of LUCC and climate change scenarios, and will provide reference for formulating adaptation strategies for better water resources management in the future. This will also benefit water diversion projects of the Luanhe River for its neighboring megacities in North China, with important implications for other water diversion projects in China and globally under a changing environment.

2. Study area and data

2.1. Study area

The Luanhe River basin is on the north of the North China Plain in the Haihe River basin, ranging from 39°02′N-42°43′N and 115°34′E-119°50′E (Fig. 1). The Luanhe River rises at the northern foot of the Bayanguertu Mountain in Zhangjiakou Prefecture of Hebei Province, flowing through 27 counties of Hebei Province, Inner Mongolia and Liaoning Province, and ending up in the Bohai Bay in Laoting County (Liu, 2012). Almost 500 tributaries flow into the pinnate Luanhe River water system along the way (Li, 2005). The Luanhe River spans 888 km controlling ~ 44,750 km^2 area, bordered by the Chaobai River and Jiyun River to the southwest and adjacent to the Bohai Sea in the south

Table 1
Previous studies on LUCC and climate change or their impacts on streamflow.

	Study area/period	Methods
Iacono et al. (2012)	Minneapolis-St. Paul, MN, USA, years between 1958 and 2005	Predicted future land use distributions from historical land use data from 1958 to 2005 based on a Markov chain
Adhikari and Southworth (2012)	Bannerghatta National Park, 1999 and 2007	Hypothetical land cover scenarios without any policy intervention were constructed by a CA-Markov model using remotely sensed data to evaluate the effects of protected areas on forest cover
Yu et al. (2011)	Daqing City, China, 1997–2007	Considering land use management, population growth, and LUCC, a system dynamic model was set up to simulate the LUCC in Daqing City driven by three different socio-economic policies
Deng et al. (2015)	Heihe River Basin in China, 2000–2010	A weather research and forecasting (WRF) model and corresponding land use and land cover data were used to simulate the indicators of water and energy balances to evaluate the impacts of LUCC
Dixon and Earls (2012)	Charlie Creek watershed in central Florida, 1976–2004	Predicted streamflow with various land use scenarios using real and simulated meteorological data to examine applicability of SWAT
Teklesadik et al. (2017)	Upper Blue Nile basin, 1981–2010 (baseline period), 2036–2065 (mid future), 2070–2099 (far future)	Analyzed the impacts of future climate change on discharge and ET using four GCMs and six hydrological models (HMs) (i.e., SWAT, SWIM, WaterGAP3, Mhm, VIC, and HBV) under different RCPs
Zhang et al. (2014)	282 catchments in China, 1960–2000	Based on a Budyko-based approach, factors (i.e., precipitation, potential ET and total water storage) that affect intra-annual ET and streamflow variability were evaluated
Aamery et al. (2016)	South Elkhorn Watershed in Lexington, Kentucky USA, 1981–2000, 2046–2065	GCM type, project phase, emission scenario, downscaling method and bias correction were selected as climate modeling factors to quantify their relative importance to choose response variables to control the variance of forecasted streamflow. Outputs of GCM and SWAT were used to simulate 112 climate realizations
Zhang et al. (2014)	Hun-Taizi River basin, northeast China, 1960–2006	The water balance model was used to project change in water yield and evaluate the effects of land cover change on runoff. Change trends and abrupt change points were identified by the Mann-Kendall method

(Shan et al., 2013; Shi, 2013). The Luanhe River basin can generally be divided into three geomorphological units, i.e., plateau, mountain, and plain, in terms of different geology, geomorphology, and formation types. The plateau topography is mainly located in the northern part of the basin with elevations ranging between 1400 and 1600 m. The mountainous regions are located on the south of the plateau and on the north of the plain, with slopes ranging between 20° and 40°. The plain is distributed in the south of the basin (Li, 2005).

The basin is characterized by decreasing temperatures from south to north ranging from 10.6 °C to −1.4 °C, and the highest and lowest temperatures appear in July and January reaching 40 °C and −26 °C, respectively (Liu, 2012). Interannual and intra-annual variations in precipitation are marked. The mean annual precipitation for the entire basin is 390–800 mm that mainly falls in July and August. In addition, the precipitation in wetter years can be 1.7–3.5 times of the driest year (Li, 2005). The dividing line of the temperate zone and warm temperate zone passes through the basin. As a result, the basin is characterized by temperate grassland and warm temperate deciduous broad-leaved forest vegetation from north to south (Li, 2005). In this study, we selected the upper reaches of the Luanhe River to evaluate the impacts of LUCC and climate change on streamflow. The Sandaohezi gauging station (hereafter termed as the SDHZ station) was selected to evaluate the change in streamflow. The drainage area of the SDHZ station is ~17,100 km², including the most afforested region in the upper reaches of the Luanhe River basin.

2.2. Data

2.2.1. Meteorological data

Meteorological data used in this study were obtained from the Meteorological Data Center of the China Meteorological Administration (http://data.cma.cn/), including annual/daily average temperature, annual/daily average maximum and minimum temperatures, annual/daily average precipitation, average daily relative humidity, average daily wind speed, daily sunshine duration and average daily vapor pressure from 1951 through 2014. The daily meteorological data during

1995–2014 were used to calculate the parameters of the weather generator to fill gaps of meteorological data. In addition, we used the China Gauge-based Daily Precipitation Analysis (CGDPA) product from 1961 to 1979 to drive SWAT. CGDPA is a daily precipitation product based on a national surface observational network with a high resolution (0.25° × 0.25° or ~27 km × 27 km) over Mainland China (Shen and Xiong, 2016).

Furthermore, we selected data sets from five GCMs: GFDL-ESM2M, HadGEM2-ES, IPSL-CM5A-LR, MIROC-ESM-CHEM and NorESM1-M (Table 2), which were bias-corrected and downscaled at a 0.5° × 0.5° spatial resolution to the WATCH Forcing Data (WFD, Weedon et al., 2011) in the fast-track of the Inter-Sectoral Impact Model Inter-comparison Project (ISI-MIP) (Liu et al., 2013). The WFD combines the ERA-40 daily data (i.e., the daily reanalysis data) and the Climate Research Unit TS2.1 data set (CRU, with observed time series of monthly variations in the climate), and the monthly mean precipitation is corrected with the Global Precipitation Climatology Centre full data set version 4 (GPCC) (Hempel et al., 2013). The ISI-MIP focuses on advancing our knowledge on climate change risks and the quantitative and cross-sectoral synthesis of different impacts of climate change, covering global water, agriculture, biodiversity and many other aspects (https://esg.pik-potsdam.de/projects/isimip2a/). The bias-corrected data sets could reflect changes in climate variability and atmosphere mean and could better investigate the effects of extreme hydrological events (Hempel et al., 2013; Leng et al., 2015). The projected meteorological data sets (i.e., daily precipitation/maximum and minimum temperatures/relative humidity/wind speed/solar radiation) from 2020 to 2030 were derived from these five GCMs.

Based on the subbasins partitioned by SWAT, the centroid of each grid cell of precipitation and subbasin was determined. Then, the value of the nearest grid cell of precipitation was taken to represent the precipitation of the subbasin. In addition, if the subbasin was large enough to cover more than one grid cell, the mean precipitation value of these grid cells were calculated and assigned to the subbasin. Finally, the precipitation was allocated to each HRU in the subbasin, i.e., precipitation of all HRUs in the subbasin is the same.
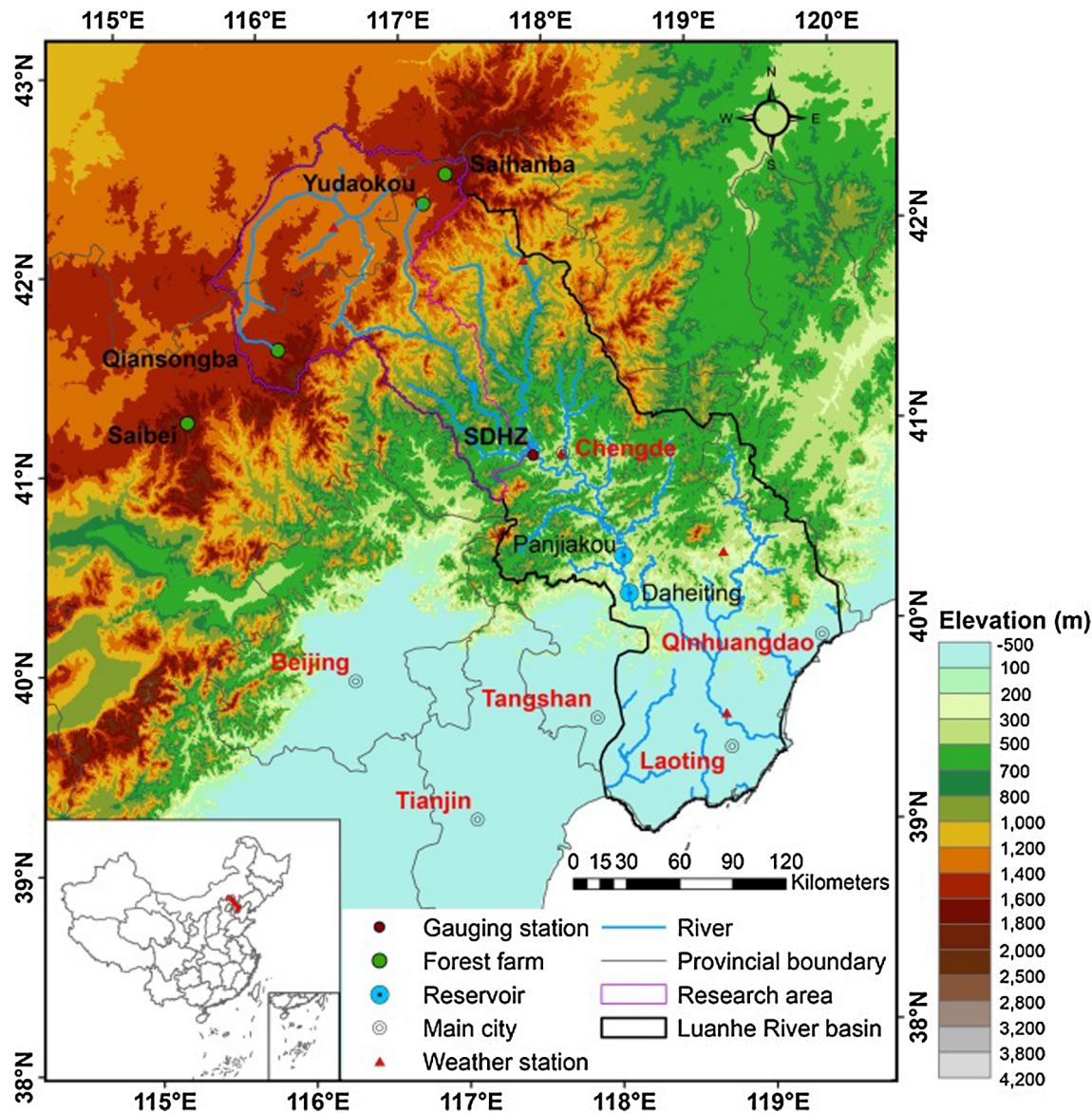
Fig. 1. Location and elevations of the Luanhe River basin, weather stations, gauging stations, forest farms, reservoirs, main cities in the Luanhe River basin, and the study area (the upper reaches shown in the pink polygon). The gauging station named Sandaohezi was abbreviated as SDHZ in the figure. (For interpretation of the references to color in this figure legend, the reader is referred to the web version of this article.)

2.2.2. Land use and other data

Six land use and land cover maps spanning from 1970 to 2014 were obtained from the Chinese Academy of Sciences. The types of land use were further divided into six categories according to the land use classification system of the Chinese Academy of Sciences, i.e.,

agriculture land, forestland, grassland, water, construction land, and unused land (Table 3). The main land use types of the Luanhe River basin include agriculture land, forestland, and grassland, accounting for more than 90% area of the entire basin. Marked LUCC has been found across the basin, featured by increased forestland but deceased

Table 2

Information on five general circulation models (GCMs) used in this study provided by ISI-MIP.

Model	Modeling center	Resolution (Lon. × Lat.)
IPSL-CM5A-LR	L'Institut Pierre-Simon Laplace	720 × 360
GFDL-ESM2M	NOAA Geophysical Fluid Dynamics Laboratory	720 × 360
HadGEM2-ES	Met Office Hadley Centre and Instituto Nacional de Pesquisas Espaciais	720 × 360
MIROC-ESM-CHEM	Japan Agency for Marine-Earth Science and Technology, Atmosphere and Ocean Research Institute (The University of Tokyo), and National Institute for Environmental Studies	720 × 360
NorESM1-M	Norwegian Climate Centre	720 × 360

agricultural and grassland. For instance, the forested area increased by ~8700 km² (~45%) during 2000–2014, yet it remained generally stable and even slightly decreased since 2010. On the contrary, agriculture land decreased considerably during 2000–2014, with the area decreased by ~3900 km² (~23%). The area of grassland also decreased, with its fraction decreasing from ~26% in 2000 to ~15% in 2014. The overall trend of land use change in the study area (upper reaches) is quite similar to the trend in the entire basin during 1970–2014; however, the trend of land use change in the study area is not that significant until 2000.

Monthly streamflow data of the SDHZ station for the period 1961–2011 were derived from Year Book of Hydrologic Data of the People's Republic of China: Hydrological Data of the Haihe River Basin. The DEM of the study region was obtained from 90 m × 90 m SRTM DEM data set V1 provided by the Cold and Arid Regions Sciences Data Center at Lanzhou, China (http://westdc.westgis.ac.cn). Soil data were derived from the Soil Database of China generated by the Nanjing Institute of Soil, the Chinese Academy of Sciences.

3. Methodology

3.1. Markov chain model and cellular automata-markov

The Markov process is a random process that a system undergoes transitions from one state to another, the properties of which include no aftereffect (i.e., the current state of a system just depends on the last adjacent period) and stability (Du et al., 2015). If both the time series and events of the process are discrete, we call the Markov process as the Markov chain (Iacono et al., 2012). Eq. (1) describes the properties of the Markov chain:

$$P \times D_t = D_{t+1} \tag{1}$$

where P is the transition probability matrix, D_t and D_{t+1} are the land use at time t and $t+1$, respectively. Each type of land use is projected by the probability p_{ij} of land use i transformed into land use j as follows:

$$p_{ij} = \frac{A_{ij}}{A_i} \tag{2}$$

$$\sum_{j=1}^{k} p_{ij} = 1 \tag{3}$$

where A_i is the total transformed area of class i over the transition period, A_{ij} is the area of land use i transformed into land use j, and k is the number of the land use types (Halmy et al., 2015; Muller and Middleton, 1994). Previous studies have shown the applicability of the Markov chain to predict land use status and change in the future (Du et al., 2015; Gao and Xu, 2010; Guo, 2006b; He et al., 2014). To build a Markov chain model, the initial state and the transition matrix need to be determined to describe the transition.

CA-Markov combines CA and the Markov chain that can predict both quantitative and spatial change of land use and land cover. The CA model is based on the previous state and simultaneously considers the state of the neighborhood cells to predict the transition (Adhikari and Southworth, 2012), despite the weakness in expressing the impacts of one cell on the entire state space. CA-Markov integrates the advantages of CA and the Markov chain to predict the land use and land cover transition more reasonably and accurately that have been widely used (Behera et al., 2012; Halmy et al., 2015; Sang et al., 2011; Subedi et al., 2013). Two constraints (i.e., slope and water body) were used to determine the suitable area of transformation from one land use type to others. Slope was considered as the constraint for agriculture land, forestland, water, and construction land, with the slope of suitable conversion area less than 15%, 65%, 1% and 25%, respectively, according to related policies and research (Behera et al., 2012). Water body was considered as the constraint for all land use types excluding water and unused land.

Constraint maps for different land uses were expressed using the Boolean map, with suitable transformation areas coded with one and others coded with zero (Behera et al., 2012; Kallali et al., 2007). Multi-Criteria Evaluation (MCE) was adopted with the Boolean intersection function to generate suitability maps for each land use type. Suitability maps for each land use are shown in Appendix B. Before prediction, the accuracy of CA-Markov should be validated. First, we predicted the land use map of 2014 with the land use maps of 2000 and 2010 as inputs, and then evaluated the predicted land use map of 2014 with the corresponding reference land use map. Kappa indices were used to

Table 3
Areas and percentages (in brackets) of land use types of the Luanhe River basin and study area (underlined values) for the period 1970–2014.

Year	Agriculture land (km²/%)	Forestland (km²/%)	Grassland (km²/%)	Water (km²/%)	Construction land (km²/%)	Unused land (km²/%)
1970	16,420 (30.3)	18,960 (35.0)	14,520 (26.8)	1,330 (2.5)	1280 (2.4)	1,710 (3.2)
	3,610 (21.9)	5,030 (30.5)	6,640 (40.3)	160 (1.0)	30 (0.2)	1,020 (6.2)
1980	16,840 (31.1)	19,340 (35.7)	14,490 (26.7)	570 (1.1)	1,260 (2.3)	1,720 (3.2)
	3,630 (22.0)	5,200 (31.5)	6,570 (39.8)	30 (0.2)	30 (0.2)	1,050 (6.4)
1995	15,730 (29.0)	23,410 (43.2)	12,180 (22.5)	710 (1.3)	1,350 (2.5)	810 (1.5)
	3,700 (22.4)	5,800 (35.1)	6,260 (37.9)	50 (0.3)	30 (0.2)	680 (4.1)
2000	17,110 (31.6)	19,140 (35.3)	14,250 (26.3)	540 (1.0)	1,350 (2.5)	1,720 (3.2)
	3,740 (22.7)	5,110 (31.0)	6,510 (39.4)	40 (0.2)	30 (0.2)	1,080 (6.5)
2010	13,490 (25.0)	27,850 (51.6)	8,150 (15.1)	560 (1.0)	3,030 (5.6)	890 (1.7)
	2,690 (16.3)	7,340 (44.5)	5,570 (33.8)	60 (0.4)	150 (0.9)	700 (4.2)
2014	13,220 (24.5)	27,800 (51.5)	8,130 (15.1)	550 (1.0)	3,140 (6.3)	890 (1.6)
	2,680 (16.2)	7,330 (44.4)	5,560 (33.7)	60 (0.4)	170 (1.0)	700 (4.2)

Table 4
Look up table of land use types.

Land use types	Agriculture land	Forestland	Grassland	Water	Construction land	Unused land
SWAT code	AGRR	FRST	PAST	WATR	URML	SWRN
SWAT plant growth database	Agriculture land-row crops	Forest-mixed	Pasture	Water	Residential-med/low density	Arid

Table 5
Description of parameters in SWAT-CUP for calibration.

Parameter name	Definition	Type[a]
SFTMP	Snowfall temperature (°C).	.bsn
SMFMX	Melt factor for snow on June 21 (mm H_2O/°C-day).	.bsn
SMFMN	Melt factor for snow on December 21 (mm H_2O/°C-day).	.bsn
ALPHA_BF	Baseflow alpha factor (days).	.gw
GW_DELAY	Groundwater delay time (days).	.gw
GWQMN	Threshold depth of water in the shallow aquifer required for return flow to occur (mm H_2O).	.gw
GW_REVAP	Groundwater "revap" coefficient.	.gw
REVAMPN	Threshold depth of water in the shallow aquifer for "revap" or percolation to the deep aquifer to occur (mm H_2O).	.gw
ESCO	Soil evaporation compensation factor.	.hru
SLOPE	Average slope steepness (m/m).	.hru
CN2	Initial SCS runoff curve number for moisture condition II.	.mgt
CH_K(2)	Effective hydraulic conductivity in main channel alluvium (mm/hr).	.rte
ALPHA_BNK	Baseflow alpha factor for bank storage (days).	.rte
SOL_AWC	Available water capacity of the soil layer (mm H_2O/mm soil).	.sol
SOL_BD	Moist bulk density (Mg/m^3 or g/cm^3).	.sol
SOL_K	Saturated hydraulic conductivity (mm/hr).	.sol

[a] Type denotes the file where the parameter is located. ".bsn": the basin file; ".gw": the groundwater file; ".hru": the HRU file; ".mgt": the HRU management file; "rte": the main channel file; and ".sol": the soil file.

evaluate the predicted land use map of 2014, including Kappa for no information (K_{no}), Kappa for location ($K_{location}$), Kappa for stratum-level location ($K_{locationStrata}$), and Kappa for standard ($K_{standard}$), with values above 80% indicating good performance of prediction (Gashaw et al., 2017; Singh et al., 2015). After the evaluation, the land use maps of 2000 and 2010 were imported into IDRISI to create the transition matrix and predict the land use in 2020 using the transition matrix, the 2010 land use map, and the suitability map.

3.2. Soil water assessment tool

SWAT is a public domain hydrologic model that can be applied from small watersheds to large river basins to simulate quantity and quality of surface and groundwater (Abbaspour et al., 2007; Dixon and Earls, 2012; Teshager et al., 2016). Time steps of simulation using SWAT can be daily, monthly and yearly (http://swat.tamu.edu/). The model has been widely used due to the solid physical mechanism that can be applied to complex large watersheds (Li, 2008; Yu et al., 2008). Input data of SWAT include DEM, soil, land use, and weather. In addition, look up tables of land use (Table 4) and soil should be written to connect with the database built in SWAT.

Parameters of the weather generator were calculated by WGNMaker 4.1 (http://swat.tamu.edu/). Here we chose Chengde, Laoting, Duolun, Qinglong, and Weichang weather stations (Fig. 1) and calculated the parameters to fill gaps in meteorological data. Inputs of WGNMaker 4.1 include daily precipitation, daily highest and lowest temperature, and daily maximum precipitation in half an hour. For lack of the daily maximum precipitation in half an hour, the data were estimated by using daily precipitation divided by 48 approximately. Daily solar radiation and dew temperatures as inputs were calculated by equations in Appendix A.

Land use scenarios in 1970 and 2020 were used in the SWAT simulation. First, under the land use scenario of 1970 and driven by the CGDPA precipitation, monthly streamflow was calibrated for the period 1961–1975 with the initial two years set as the warm-up period, and validated for the period 1976–1979. In order to fully calibrate the model under the 1970 land use and ensure that the year 1970 was included during calibration, we selected the longer period 1963–1975 for calibration and the period 1976–1979 for validation, given that the streamflow was influenced significantly by human activities after the 1980s. The model was calibrated manually and automatically using the

SUFI-2 algorithm by SWAT-CUP and 16 parameters were selected and identified (Table 5). The coefficient of determination (R^2) and Nash-Sutcliffe efficiency coefficient (E_{ns}) were used to evaluate the model performance. However, the spring flood in April at the SDHZ station could not be simulated well by SWAT, because the spring flood is more related to river thawing (recorded by Year Book of Hydrologic Data of the People's Republic of China: Hydrological Data of the Haihe River Basin) whose mechanism is not depicted in this model. Therefore, we proposed an empirical method to correct for the poor simulations of spring flood in April (see Section 4.3).

Second, we used the outputs from five GCMs under four RCPs and the 2020 land use scenario to drive SWAT and simulate streamflow during 2020–2030. Third, we used the land use map of 1970 to replace the land use map of 2020, and simulated streamflow for the same period to quantify the impacts of LUCC on runoff. Note that when the land use map was changed from 2020 to 1970, the initial parameters of SWAT related to land use (i.e., CN2) were subsequently adjusted automatically (e.g., the area weighted average of CN2 for a subbasin is 68 in 2020 and 78 in 1970). Given the calibrated value of the relative change in CN2 (e.g., −10%), the initial value of CN2 can be adjusted automatically under a different land use scenario. Therefore, CN2 values under different simulation scenarios are changed accordingly with land use maps.

4. Results

4.1. Projected precipitation from general circulation models

Precipitation plays a critical role in runoff simulation, and the variability in precipitation leads to a complicated hydrological regime (Houston, 2006; Moulin et al., 2008; Saifullah et al., 2016). For ease of expression, outputs from different GCMs under RCPs are hereafter referenced to as the combination of the abbreviated names of GCMs and the representative numbers of RCPs (e.g., GFDL26 represents the output from GFDL-ESM2M under the RCP2.6 scenario). The projected precipitation by the five GCMs under four RCPs for the study area (the upper reaches of the Luanhe River basin) shows the mean annual precipitation of 458 mm (4% increase), 458 mm (4% increase), 444 mm (1% increase) and 470 mm (7% increase) under RCP2.6, RCP4.5, RCP6.0, and RCP8.5, respectively, relative to the mean annual precipitation of 441 mm from CGDPA precipitation for the baseline period
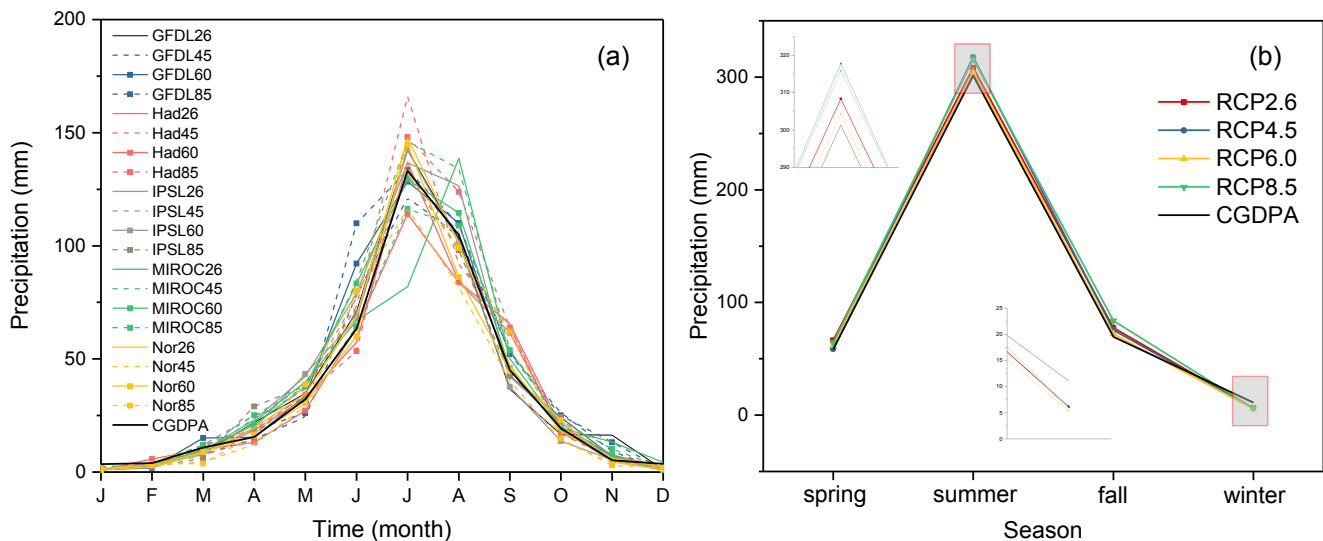
Fig. 2. (a) Mean monthly precipitation among the five GCMs and four RCPs for the period 2020–2030. The mean monthly precipitation from CGDPA (black) was calculated for the period 1961–1979; and (b) Seasonal precipitation under four RCPs and from CGDPA data.

1961–1979. The precipitation is mainly concentrated in July and August, and some of the future precipitation (e.g., Had45, Had85 and Nor26) is much higher than the historical level reflected by CGDPA data for the period 1961–1979, implying large possibility of flooding in summer in the future. Specifically, July shows the highest monthly precipitation in a year among all the GCMs and RCP scenarios except MIROC26 showing the highest precipitation in August (Fig. 2a).

The basin belongs to the warm temperate zone monsoon climate with four distinct seasons, characterized by hot and rainy summer, cold and dry winter, and dry spring. We looked into projected seasonal precipitation, i.e., spring (i.e., MAM), summer (i.e., JJA), fall (i.e., SON), and winter (DJF). The mean precipitation from all GCMs and RCPs for the period 2020–2030 in the four seasons is 63 mm (9% increase), 312 mm (4% increase), 77 mm (10% increase), and 6 mm (45%

decrease), respectively, compared with the observed mean precipitation of 58 mm, 301 mm, 70 mm, and 11 mm in the four seasons from CGDPA data (1961–1979) (Fig. 2b). The strongest increase and decrease in precipitation occur in fall under RCP8.5 and in winter under RCP6.0, showing relative differences of 20% and −52%, respectively, compared with the CGDPA precipitation (1961–1979). The decrease in precipitation only occurs in winter (-45%, −43%, −52%, and −45% for RCP2.6, RCP4.5, RCP6.0 and RCP8.5, respectively), and the other seasons become wetter (Figs. 2b and 3). Variations in atmospheric general circulation in East Asia and the Okhotsk Sea are related to the changing precipitation in spring and summer in the North China Plain (Ma et al., 2010).
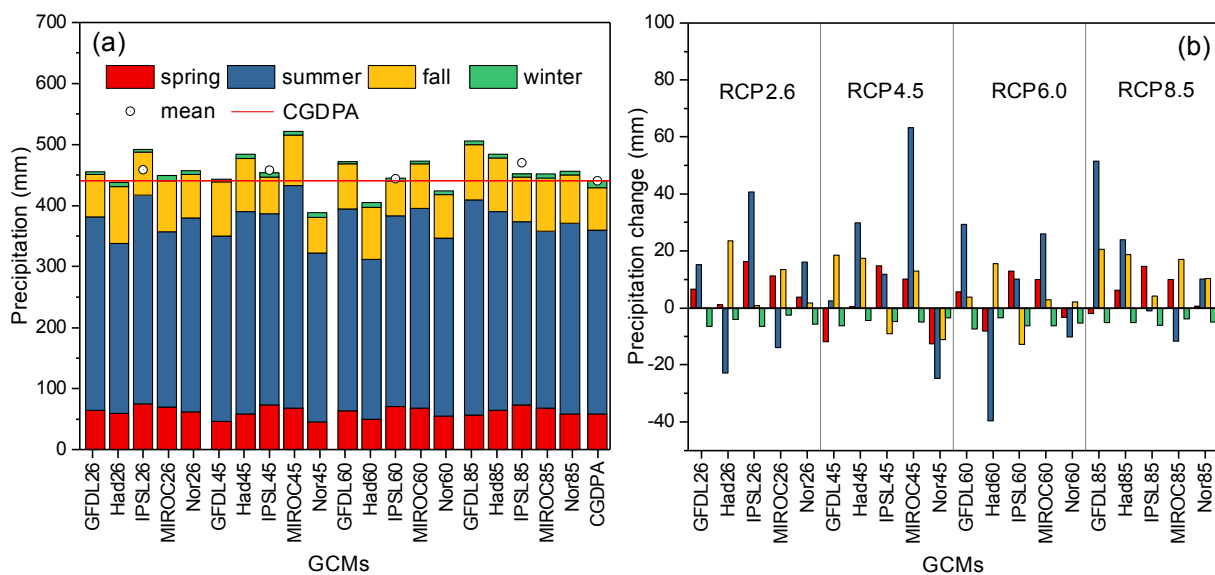

Fig. 3. (a) Mean annual precipitation and its seasonal contributions from five GCMs under four RCPs for the period 2020–2030, and the mean values denote the mean annual precipitation for all GCMs for each RCP as well as the mean annual precipitation from CGDPA (the red line and the last bar) for the period 1961–1979; and (b) variations in seasonal precipitation from five GCMs under four RCPs for the period 2020–2030 with respect to CGDPA for the period 1961–1979. Positive (negative) values denote increases (decreases) in precipitation for the period 2020–2030. (For interpretation of the references to color in this figure legend, the reader is referred to the web version of this article.)
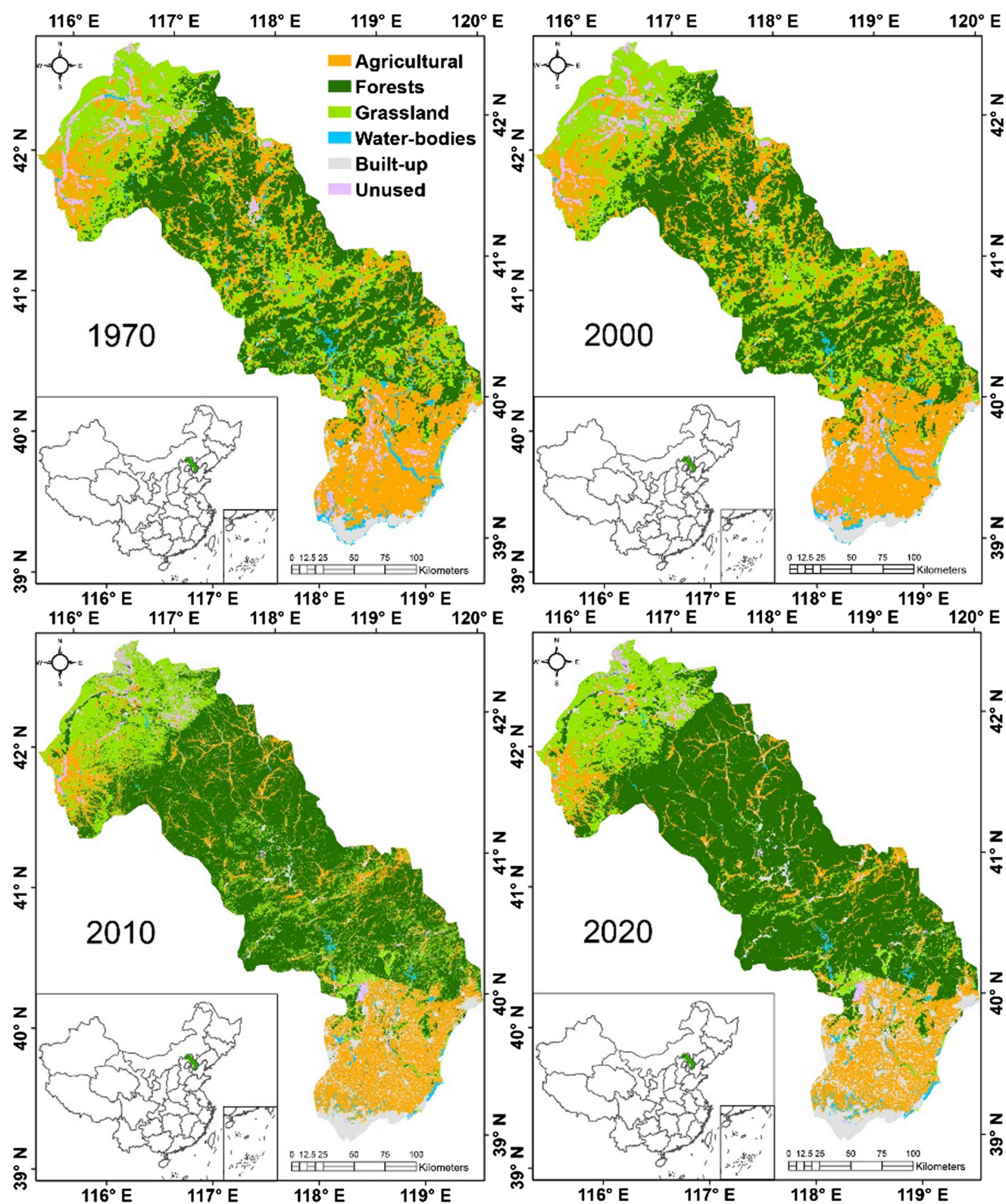
Fig. 4. Land use maps of the Luanhe River basin in 1970, 2000, 2010 and 2020 (predicted using CA-Markov).
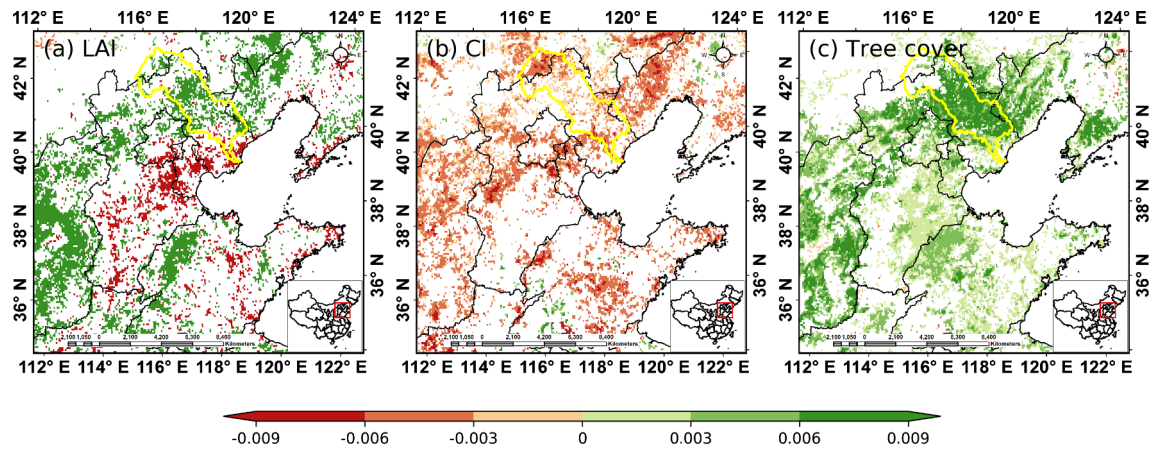
Fig. 5. Change rates of (a) MODIS leaf area index (LAI), (b) clumping index (CI), and (c) MODIS tree cover from 2001 to 2016. Yellow polygons show the boundary of the Luanhe River basin. (For interpretation of the references to color in this figure legend, the reader is referred to the web version of this article.)

Table 6
Comparison between land use scenarios of 1970 and 2020.

	Entire Luanhe River basin			Study area (upper reaches)		
	1970 (km²/%)	2020 (km²/%)	Relative change/%	1970 (km²/%)	2020 (km²/%)	Relative change/%
Agriculture	16,420 (30.3)	11,580 (21.5)	−29.5	3610 (21.9)	2320 (14.1)	−35.7
Forestland	18,960 (35.0)	29,640 (55.0)	56.3	5030 (30.5)	7570 (45.9)	50.4
Grassland	14,520 (26.8)	7310 (13.6)	−49.7	6640 (40.3)	5750 (34.9)	−13.4
Water	1330 (2.5)	740 (1.4)	−44.4	160 (1.0)	80 (0.5)	−52.5
Construction	1280 (2.4)	3930 (7.3)	207.0	30 (0.2)	210 (1.3)	513.4
Unused land	1710 (3.2)	720 (1.3)	−57.9	1020 (6.2)	570 (3.5)	−43.8

4.2. Prediction of land use change

4.2.1. Prediction of the land use scenario in 2020

Based on the land use transition matrix from 2000 to 2010 and the land use map in 2010 as well as the suitability map, the land use map of 2014 was simulated using CA-Markov. Then the Kappa indices were used to validate the accuracy of CA-Markov by comparing the simulated land use map with the observed land use map in 2014, showing K_{no} of 86.2%, $K_{location}$ of 84.5%, $K_{locationStrata}$ of 84.5%, and $K_{standard}$ of 82.2% all higher than 80%. This indicates good projections of land use in the future (Behera et al., 2012).

We used CA-Markov and the land use maps in 2000 and 2010 to predict the land use scenario in 2020 (Fig. 4). Before 2000, the land use in the Luanhe River basin changed slowly with limited change areas of different land use types. During 2000–2014, the land use changed

dramatically, particularly for forestland, grassland, and agriculture land, with the proportion changed by 16%, 11%, and 7%, respectively. From 2000 to 2010, the areas of grassland and agriculture land decreased at a rate of ~610 km²/yr and ~360 km²/yr, respectively, but the area of forestland increased at a rate of ~870 km²/yr. We further analyzed changes in the 8-day leaf area index (LAI), 8-day clumping index (CI), and annual tree cover from MODIS data for the period 2001–2016 (Fig. 5). The LAI in most of the Luanhe River basin increased from 2001 to 2016, indicating a denser vegetation. The CI decreased, indicating that leaves become more clumped. Both the increased LAI and decreased CI are attributed to the increasing proportion of tree cover (Fig. 5(c)), because the LAI of trees is often larger than herbaceous vegetation and therefore shows lower CI values.

Hebei Province implemented the afforestation project since 1999 in Zhangjiakou and Chengde Cities and this project will continue by 2021.

Table 7
Land use transition matrix of the study area for the period 1970–2020.

		2020					
		Agriculture land (km²)	Forest (km²)	Grassland (km²)	Water (km²)	Construction land (km²)	Unused land (km²)
1970	Agriculture land	1537	797	1114	17	106	38
	Forest	124 (−6 7 3)	4461	407	12	5	21
	Grassland	395 (−7 1 9)	2064 (1657)	3784	20	57	320
	Water	56 (39)	50 (38)	15 (-5)	19	3	17
	Construction land	5 (−1 0 1)	3 (−2)	4 (−5 3)	1 (−2)	21	0
	Unused land	204 (1 6 6)	192 (1 7 1)	427 (1 0 7)	8 (-9)	14 (14)	178

Note: The values in parentheses mean the net area of land use types in 1970 converted into land use types in 2020, e.g., the value of −673 is the net area that the forest in 1970 is converted into agriculture land in 2020. This value was calculated by the area of forest converted into agriculture land (i.e., row 2 and column 1 in the table: 124 km²) minus the area of agriculture land in 1970 converted into forest in 2020 (i.e., row 1 and column 2 in the table: 797 km²).
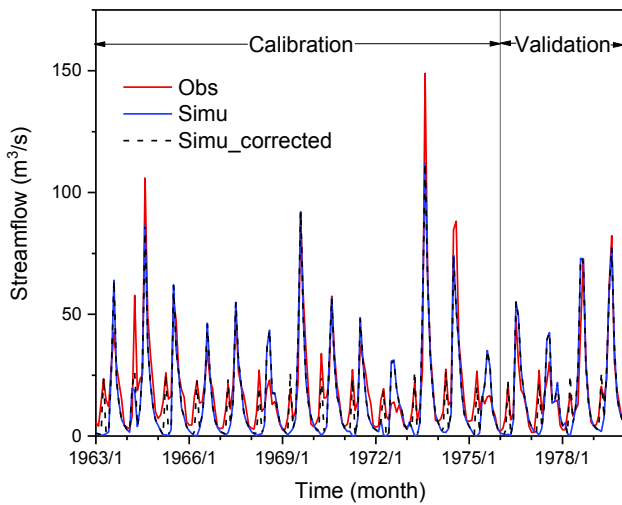
Fig. 6. Observed and simulated monthly streamflow at the SDHZ station for the calibration period (1963–1975) and validation period (1976–1979). The simulated spring flood during both calibration and validation periods (i.e., the period 1963–1979) was corrected using equation (4).

The forest coverage rate at three tree farms (i.e., the Saibei Tree Farm at Zhangjiakou, Qiansongba Tree Farm at Fengning County in Chengde, and Yudaokou Tree Farm at Weichang County in Chengde) is expected to reach ~73%. Nowadays, the forest coverage rate of Chengde has increased to ~57%, which is highest in North China and its surrounding mountainous areas (Fig. 5). These tree farms function as the first barrier against sandstorms in North China and have largely defended Beijing from the sandstorm during recent years. Furthermore, forests enhance the capacity of rainfall retention by conserving water through canopy and vegetation, soil, and litter layer under it. Most of the conserved rainfall infiltrates and may contribute more lateral flow over the mountainous region (see Section 4.4.2).

4.2.2. Comparison of land use scenarios between 1970 and 2020

Here we compared the land use scenario in 2020 predicted by CA-Markov and the land use scenario in 1970, both of which were used to
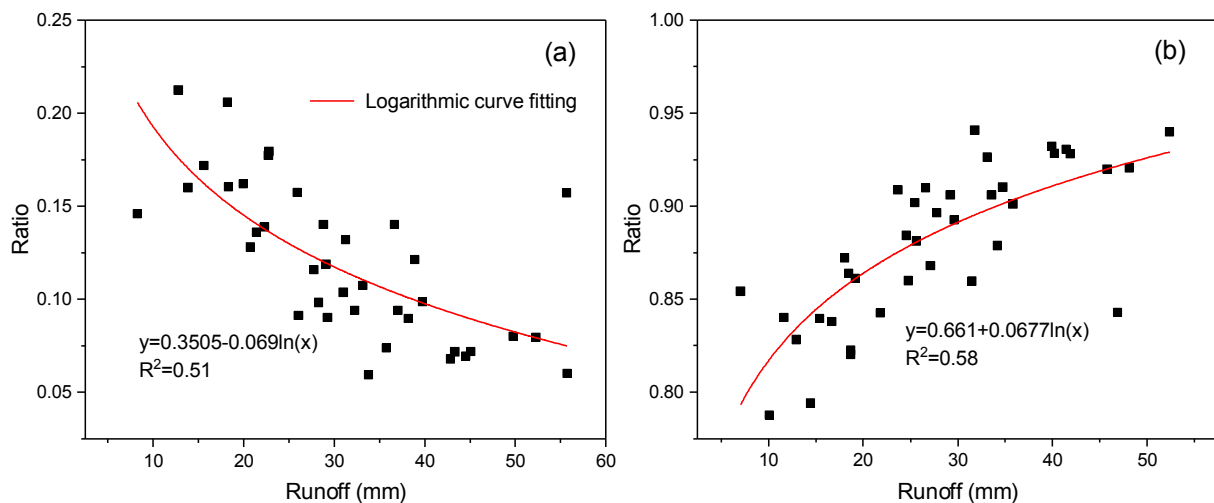

Fig. 8. Boxplots of annual/seasonal runoff simulations under four RCPs during 2020–2030. The number on top of each box represents the mean value of the annual or seasonal runoff, corresponding to the solid square in the box. The line in the box is the median, and the bottom and top edge of the box represent the 25th and 75th percentiles, respectively. The circles are outliers beyond the range from "25th percentile − (1.5 × interquartile range)" and "75th percentile + (1.5 × interquartile range) ".

simulate the future runoff and evaluate the impacts of LUCC on runoff. Comparison shows that the areas of forestland and construction land increase but agriculture land, grassland, water bodies, and unused land decrease (Table 6). Across the entire Luanhe River basin, the proportion of grassland decreases from ~27% in 1970 to ~14% in 2020, with the area decreased by ~7200 km². In contrast, the forestland increases by ~10,700 km² with the proportion increased from ~35% to ~55%. Relative changes in water, construction land, and unused land are marked, but the proportions of them are small such that the changes may have less impact on runoff. Change trends in land use types in the study area (the upper reaches) are similar to those in the entire basin. However, the magnitude of change in grassland in the study area (−13%) is much smaller than that in the entire basin (−50%).

Furthermore, we calculated the transition matrix for the period

Fig. 7. (a) Logarithmic relationship between the total runoff in a year and the ratio of spring flood to total runoff in a year; and (b) the logarithmic relationship between the total runoff in a year excluding the runoff in April and the ratio of it to the total runoff in a year.
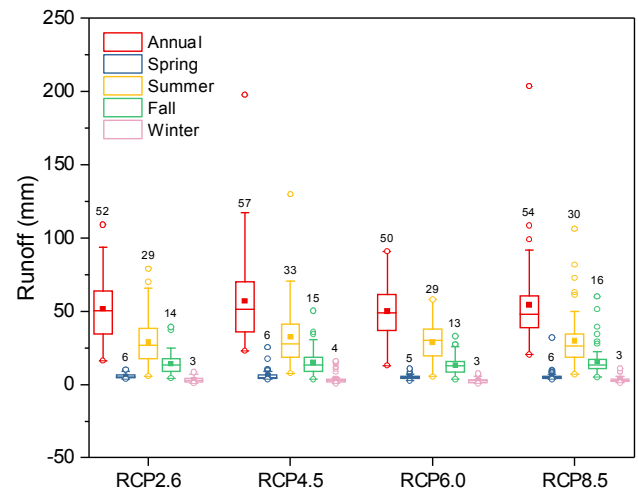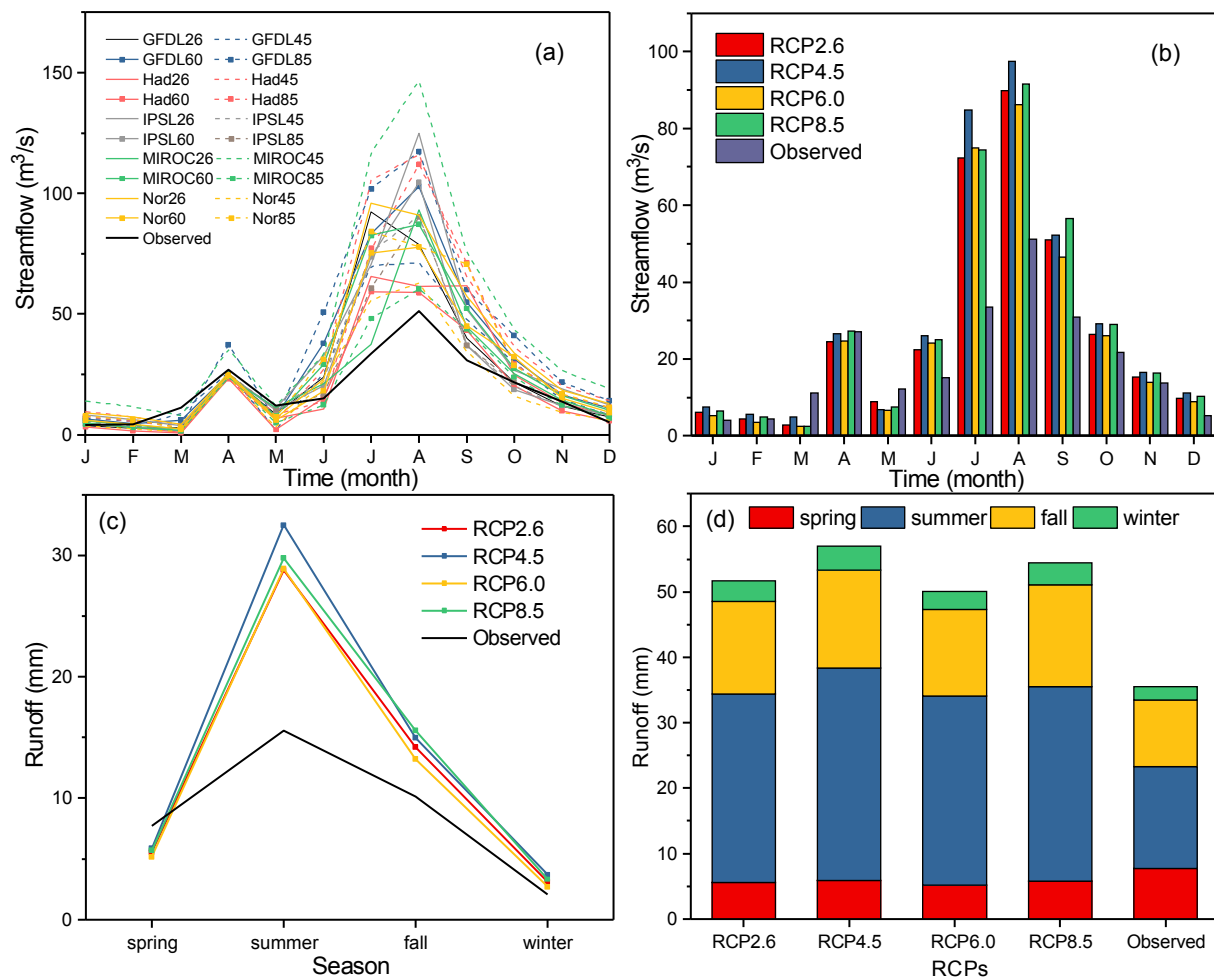
Fig. 9. (a) Mean monthly predicted streamflow under five GCMs and four RCPs during the period 2020–2030; (b) mean monthly predicated streamflow for all GCMs under each RCP during the period 2020–2030; (c) ensemble means of runoff depths from all GCMs in four seasons under each RCP; and (d) mean annual runoff depths and its seasonal contributions for all GCMs under each RCP. The observed streamflow was calculated for the period 1961–1979.

1970–2020 (Table 7) in the study area to develop a better understanding of the connection between LUCC and possible changes in the hydrological regime. Results show that the increasing area in forestland is mainly transformed from grassland ($\sim 1700\,km^2$) and agriculture land ($\sim 700\,km^2$). Meanwhile, some of the agriculture land and the unused land are transformed into grassland, so that even though a large proportion of grassland is transformed into forest, only a relatively small net decrease in grassland occurs (i.e., a relative change of -13%). Furthermore, the areas of water, construction land, and unused land change remarkably. The increasing construction land would increase more impervious surfaces, and more rainfall would therefore be converted into surface runoff. Both afforestation and urbanization promote the transformation among different land use types and influence runoff in the basin profoundly.

4.3. Model calibration and validation and correction for simulated spring flood

The SWAT model was calibrated for the period 1961–1975 with the initial two years as the warm-up period and validated for the period 1976–1979. Prior to correction for simulated spring flood, R^2 and E_{ns} for the calibration period are 0.74 and 0.67, respectively, and are 0.80

and 0.71 for the validation period, respectively (Fig. 6). Note that the higher metrics of the validation than those of the calibration are in part related to the sample size, with 156 and 48 during the calibration and validation periods, respectively. Some studies also have shown similar results of higher metrics in a shorter validation period than those for a longer calibration period (Shawul et al., 2013; Thampi et al., 2010). Even though the values of metrics are acceptable for both calibration and validation periods, the spring flood in April could not be simulated well. We assume that the spring flood is associated with the total runoff in a year. Our analysis indicated that the ratio of observed spring flood to total runoff has a significant logarithmic correlation with the annual runoff during 1963–2000 (Fig. 7(a)). To correct for the simulated future spring flood, the relationship mentioned above needs to be translated into the relationship between the total runoff in a year excluding the runoff in April and the ratio of it to the total runoff in a year (Fig. 7(b)) (e.g., assuming that the spring flood in a year is 10 mm and the total runoff in a year is 50 mm, the relationship was built between the ratio of 0.8 (40/50) and 40 mm). The mean annual ratio of spring flood to total runoff in a year from 1963 to 2000 was found to be 0.12, so it was set as the upper bound for correcting for the simulated spring flood if the ratio of the total runoff excluding spring flood was greater than one. The ratio of spring flood was corrected by:
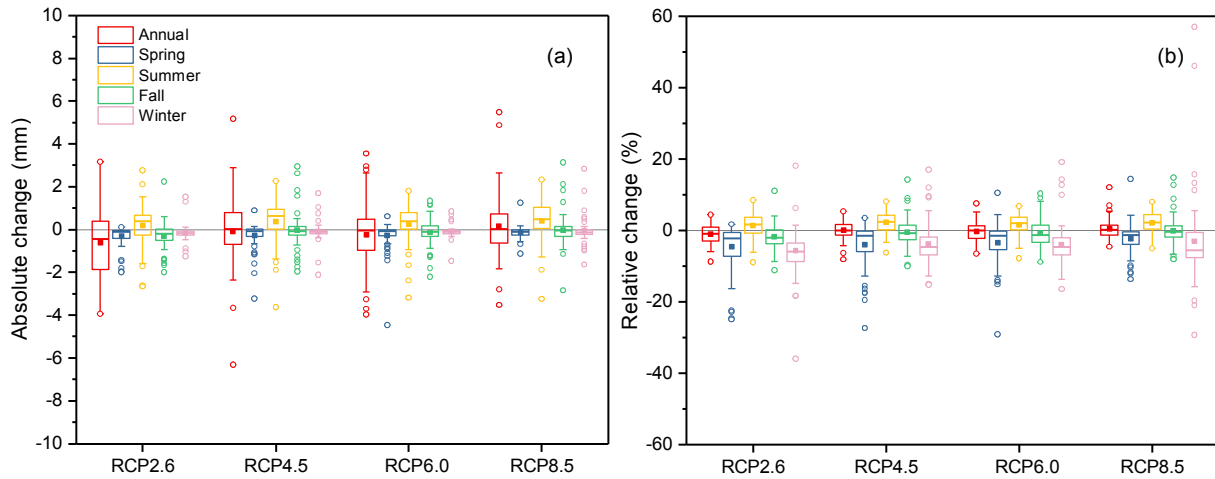
Fig. 10. Boxplots of (a) absolute change ($F_{2020} - F_{1970}$), and (b) relative change of runoff ($F_{2020} - F_{1970}$)/F_{1970} under different land use scenarios. F_{1970} and F_{2020} are the simulated runoff for the period 2020–2030 under the 1970 and 2020 land use scenarios, respectively. The description of symbols in this figure is the same as Fig. 8.

$$R = \begin{cases} 1 - (0.0677\ln(x) + 0.661), & x < 150 \\ 0.12, & x \geq 150 \end{cases} \tag{4}$$

where x represents the annual runoff excluding the spring flood (mm), and R represents the ratio of spring flood to total runoff in a year. Based on Eq. (4), the simulated spring flood was corrected during the period 1963–2011 and validated during the period 2001–2011. After the correction for simulated spring flood, the values of R^2 and E_{ns} for calibration of SWAT are 0.81 and 0.78, and for validation are 0.88 and 0.82, respectively. Moreover, we simulated spring flood from 2001 to 2011 using the same parameters during model calibration and corrected for it. Results show that the correction for the simulated spring flood is effective, indicating that the root mean square error for the period 2001–2011 decreases from $14 \, \text{m}^3/\text{s}$ to $7 \, \text{m}^3/\text{s}$. Therefore, the parameters of SWAT for the calibration period and the method of correcting for the simulated spring flood in April were jointly used to simulate streamflow from 2020–2030 using the precipitation outputs from five GCMs under four RCPs.

4.4. Predicting runoff for the period 2020–2030 under different land use and climate change scenarios

4.4.1. Under the 2020 land use and different climate change scenarios

Based on the calibrated model, runoff under the land use scenario in 2020 during 2020–2030 was simulated and compared to the simulated runoff under the land use scenario in 1970 (see Section 4.4.2), assuming that the responsive relationship between climate variables and runoff will remain the same (Kamga, 2001). The projected runoff under the 2020 land use scenario varies with different RCPs (Fig. 8). The maximum (57 mm) and minimum (50 mm) mean annual runoff depths are under RCP4.5 and RCP6.0, respectively, with RCP8.5 (54 mm) and RCP2.6 (52 mm) in between. All these simulated runoff depths in the future are higher (39%-58%) than the observed mean annual runoff of 36 mm for the baseline period (1961–1979). Furthermore, the streamflow extremes become more intense, showing the maximum mean monthly streamflow during 2020–2030 of more than $80 \, \text{m}^3/\text{s}$ under four RCPs (occurring in July or August) (Fig. 9(b)), compared with the observed maximum mean monthly streamflow of $\sim 50 \, \text{m}^3/\text{s}$ from 1961 to 1979. Certain measures may therefore be taken to reduce possible flood disasters, including enhancing the discharge capacity of river

channels and better managing the operation of reservoirs to adapt to the increasing streamflow and realize the maximum benefits of reservoirs (Middelkoop et al., 2001).

Moreover, mean monthly runoff simulations during 2020–2030 for five cases (GFDL26, Had26, Had60, Nor26 and Nor85) show the maximum in July, but those for the other 15 cases occur in August, consistent with the timing of the observed mean monthly streamflow during 1961–1979 (Fig. 9). The mean summer runoff depth increases most significantly, showing 32 mm under RCP4.5, 100% higher than the observed mean seasonal runoff depth of 16 mm for the period 1961–1979. Overall, the mean seasonal runoff depth for the period 2020–2030 is higher than the observed runoff for the period 1961–1979 except in spring (Fig. 9(c)).

Although precipitation only decreases in winter, runoff decreases in spring, suggesting that the change in runoff is not determined only by precipitation. Changes in ET and vegetation may also influence the variation in the simulated runoff, and the increased forestland can be an important factor. The mean annual runoff coefficient in spring and winter is ~0.1 and ~0.5 during 2020–2030, respectively, compared to ~0.1 and ~0.2 for the period 1961–1979. The increased future runoff coefficient in winter may be related to the increased future precipitation in summer and fall, which may lead to soil moisture storage replenished greatly and more runoff generated in winter (Brown et al., 2013). In addition, the decreased runoff in spring in the future may also be related to the uncertainty in the correction for the simulated spring flood to some degree.

4.4.2. Under the 1970 land use and different climate change scenarios

Here we simulated runoff under the 1970 land use and compared it with that under the 2020 land use scenario (Fig. 10). Results show that the predicted runoff for the period 2020–2030 under the 2020 land use scenario is generally lower than that under the 1970 land use scenario, indicating that the LUCC from 1970 to 2020 is likely to reduce runoff. The mean annual runoff depths from the five GCMs for the period 2020–2030 under the 1970 land use scenario are 52.3 mm, 57.1 mm, 50.3 mm and 54.3 mm for the four RCPs, respectively, slightly higher than those under the 2020 land use scenario (51.7 mm, 57.0 mm, 50.0 mm, and 54.3 mm). In general, the land use change can result in increases or decreases in runoff in different years in the future. The LUCC (i.e., more forestland but less agriculture land) would lead to
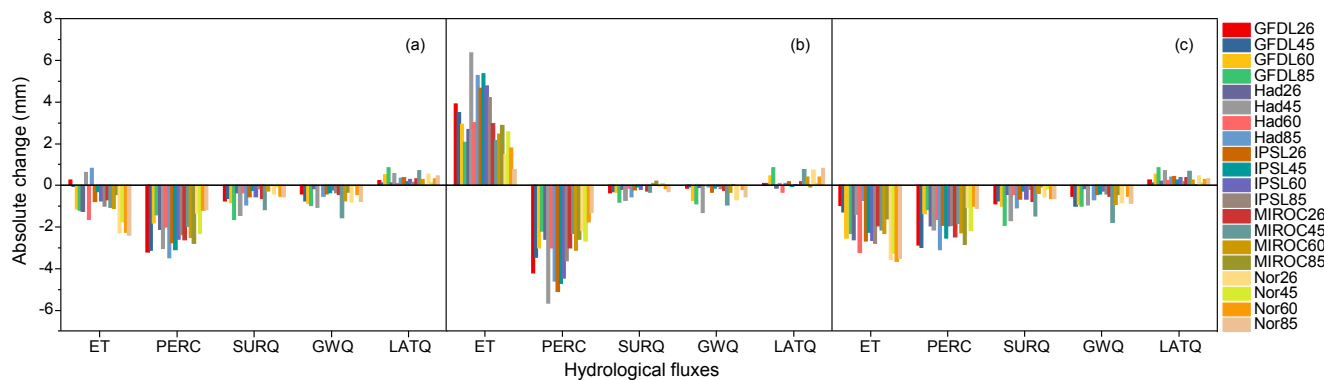
Fig. 11. (a) Absolute changes (the values under the 2020 land use scenario minus the values under the 1970 land use scenario) of mean annual ET, water percolation past bottom of soil profile (PERC), surface runoff generated in the watershed (SURQ), groundwater contribution to stream (GWQ), and the lateral flow contribution to streamflow in watershed (LATQ) between the 2020 land use scenario and the 1970 land use scenario for the entire study area; (b) the same as (a) but for subbasins with changes in water area less than 50%; and (c) the same as (a) but for subbasins with changes in water area greater than 50%.
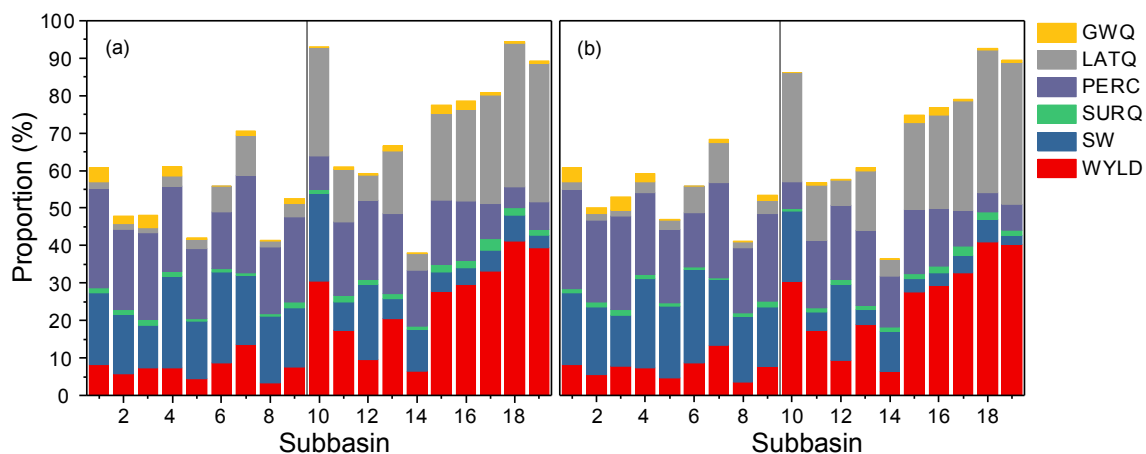

Fig. 12. Averaged proportions of the mean annual values of six outputs: groundwater contribution to streamflow (GWQ), lateral flow contribution to streamflow (LATQ), water that percolates past the root zone (PERC), surface runoff generated in the watershed (SURQ), soil water content (SW) and water yield (WYLD) (i.e., the net amount of water that leaves the subbasin and contributes to streamflow) to the corresponding mean annual precipitation among 20 cases (5 GCMs × 4 RCPs). (a) and (b) Represent the proportions under the 1970 and 2020 land use scenarios, respectively. The vertical black line in both figures partitions the subbasins into the plateau (i.e., subbasins Nos. 1–9) and mountainous regions (i.e., subbasins Nos. 10–19).

decreases in runoff in spring, fall and winter, but increases in summer, resulting in slightly decreased mean annual runoff relative to the 1970 land use scenario. This highlights that the future change in runoff over this basin is likely to be dominated by climate change, though considerable LUCC would be taking place.

The impacts of forest on runoff are mainly realized through affecting canopy interception, infiltration, and ET processes. Previous studies have found that the land use/land cover transition would lead to changes in ET and infiltration and consequently changes in water to regional aquifers (Baker and Miller, 2013; Baldyga et al., 2008). Some studies pointed out that decreases in forestland cause increases in runoff (Siriwardena et al., 2006) or water yield (Zhang et al., 2014). To further look into the reason for the change in runoff, we set up a new SWAT project with the SDHZ station as outlet, for which the precipitation of the study area remained constant under the two land use scenarios, as different land use scenarios would result in different partitioning of HRUs (e.g., 280 and 291 HRUs for the 1970 and 2020 land use scenarios in our study area, respectively) and therefore different hydrological response mechanisms. This analysis reduced the impact of neighboring subbasins and only focused on the change in

hydrological response within the study area. Changes in multiple runoff components caused by LUCC in our study area under 20 scenarios (5 GCMs × 4 RCPs) were analyzed.

Absolute changes in mean annual ET, water percolation past bottom of soil profile (PERC), surface runoff generated in the watershed (SURQ), groundwater contribution to stream (GWQ), and lateral flow contribution to streamflow in watershed (LATQ) during 2020–2030 were calculated (Fig. 11). It was found that for the entire study basin, total runoff and PERC decreased, which is attributed to the afforestation and consistent with published studies on the impact of afforestation on runoff in North China (Liang et al., 2015). Furthermore, runoff components including SURQ and GWQ decrease, but the LATQ increases due to the LUCC.

Moreover, the decrease in ET for some subbasins is mostly attributed to the marked reduction in water area. We compared changes in the hydrological fluxes mentioned above between subbasins with changes in water area less than 50% (SUB1) (SUB1 accounting for 26% of the study area) and subbasins with changes in water area larger than 50% (SUB2). The decreased water area mainly occurs in SUB2 from 124 km² in the 1970 land use scenario to only 40 km² in the 2020 land
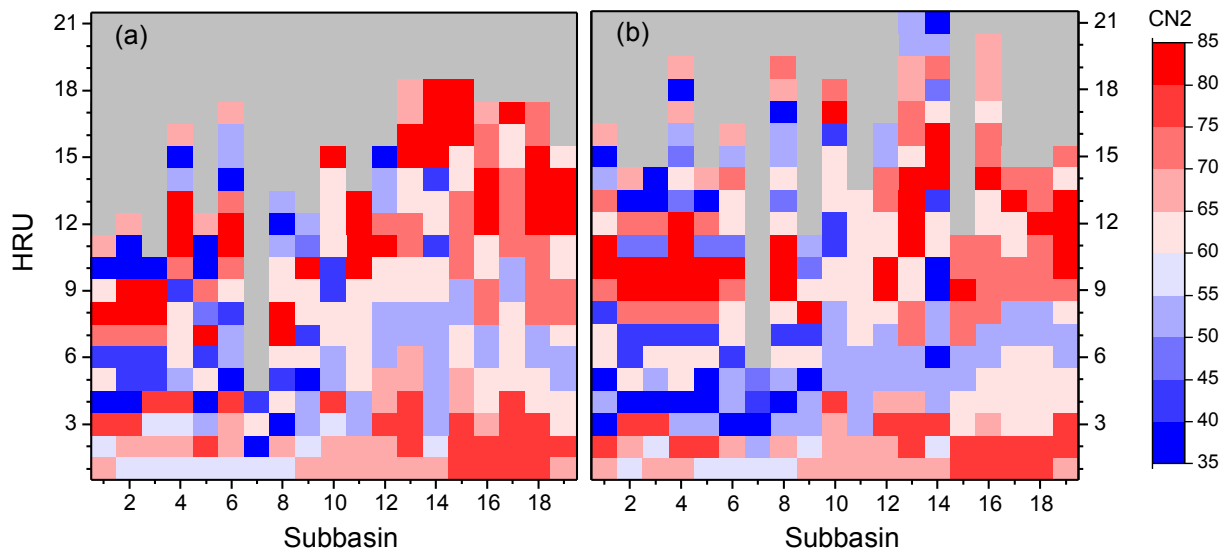
Fig. 13. Soil conservation service (SCS) curve numbers under average moisture (CN2) of each HRUs for the 1970 land use (a) and 2020 land use (b). The X axis represents the ID numbers of subbasins and the Y axis represents the ID numbers of HRUs in each subbasin.

use scenario, but the water area keeps generally stable in SUB1. Results indicate that the mean annual ET under 20 cases (5 GCMs × 4 RCPs) increases by ∼3 mm in SUB1 (Fig. 11(b)) but decreases by ∼2 mm in SUB2 (Fig. 11(c)), and trends in other hydrological fluxes are similar for both SUB1 and SUB2. Given that the proportion of water area for SUB2 is larger than SUB1, the variation in ET is dominated by SUB2 and therefore shows a decrease in ET across the entire study basin caused by LUCC.

We further selected a subbasin without water bodies and compared the change in hydrological fluxes resulting from LUCC (i.e., more forestland but less grassland, with agriculture land stable) under the 20 cases. Results show that ET and LATQ increase by up to ∼6 mm and ∼1 mm, respectively, but PERC, GWQ and SURQ decrease by up to ∼6 mm, ∼4 mm and ∼0.9 mm, respectively. Therefore, it can be speculated that the decrease in ET cross the study basin is likely related to the decrease in water area. The increase in forestland and decrease in both agricultural land and grassland can jointly result in decreases in PERC, SURQ, and GWQ, but increases in ET and LATQ in our study area. Description of the ET process for water bodies in SWAT needs to be further improved by considering the water balance so as to reduce the overestimation of ET for subbasins with water bodies, which may counteract the effect of afforestation on ET when water bodies decrease.

5. Discussion

5.1. Impacts of increased forestland on runoff

Quantifying the impacts of changes in forestland on water availability is of great importance to understand hydrological processes for regions with marked afforestation or deforestation, and thereby to the implementation and assessment of ecological restoration projects. Some studies reveal that the impacts of forests are associated with the area of basin and mainly exert on the baseflow (Shi and Li, 2001). During low flow season, the decrease in forestland reduces ET and interception, and then results in increases in soil water content and groundwater recharge, finally resulting in the increase in low flow (Zhang and Wei, 2012). In our study area, the increased forestland results in more LATQ, though SURQ, GWQ, and streamflow all decrease. Lateral flow is

dominant for hill slope topography, and plateau is considered to be inactive in the rainfall-runoff process (Hoang et al., 2017; Savenije, 2010). Furthermore, mountain regions with hill slopes are mostly forested and plateaus with modest slopes are distributed with grassland and agricultural land (Savenije, 2010). So the increased forestland mainly occurs in the mountainous region and the deeper root of forests can facilitate generation of interflow produced by infiltrated water (Becker and Mcdonnell, 1998).

We analyzed the rainfall-runoff mechanism of the upstream plateau (i.e., subbasins Nos. 1–9) and the downstream mountainous region (i.e., subbasins Nos. 10–19). First, the mean annual values of six outputs: GWQ, LATQ, PERC, SURQ, soil water content (SW), and water yield (WYLD) (i.e., the net amount of water that leaves the subbasin and contributes to streamflow) under 20 cases (5 GCMs × 4 RCPs) were extracted from outputs of each subbasin. Then, the proportion of the six outputs to the corresponding mean annual precipitation (the proportion of GWQ/LATQ/PERC/SURQ/SW/WYLD hereinafter) was calculated and averaged among 20 cases under the 1970 (Fig. 12(a)) and 2020 (Fig. 12(b)) land use scenarios, respectively.

In general, the proportions of PERC and SW are higher in the plateau (i.e., the left half part of Fig. 12(a) and (b)) and proportions of LATQ and WYLD are higher in the mountainous region (i.e., the right half part of Fig. 12(a) and (b)). This indicates that plateau is dominated by the vertical hydrological process (i.e., evaporation and percolation) and the mountainous area is active in the rainfall-runoff process to generate more lateral flow and runoff. In addition, the proportions of six outputs except GWQ in the plateau slightly increase under the 2020 land use scenario compared to those under the 1970 land use scenario, but the proportions of the six outputs except LATQ decrease in the mountainous region. This indicates that topography also plays a marked role in regulating hydrology processes and further reflects in the impacts of LUCC on runoff components.

The LUCC (i.e., from the 1970 to 2020 land use scenario) shows a consistent trend spatially except grassland that increases in the plateau, but decreases in the mountainous region that has been transformed into forestland. This may be the main reason for the increased PERC and SW and decreased GWQ on the plateau arising from LUCC. That is to say, topography influences the change pattern of LUCC to some degree.

Agricultural land and grassland are often distributed on the plateau with modest slopes, and the mountainous region with hill slopes is forested. Therefore, the amplitude and trend in LUCC vary with regions of different topography. On the other hand, different rainfall-runoff mechanisms for the plateau and mountainous regions further amplify or counteract the impacts of LUCC on runoff (e.g., lateral flow is the dominant runoff component in the mountainous region. Though the LUCC reduces water yield, the lateral flow still increases). Also, topography influences the spatial distribution of climate variables (i.e., precipitation and temperature), which needs to be well considered for regional climate projection (Savenije, 2010).

Given the unique topography in our study area with the plateau and mountain regions distributed from the upper reaches to the gauging station, lateral flow accounts for a large proportion of the simulated runoff and therefore determines the change in streamflow. Note that LUCC increases runoff in summer (~ 0.3 mm) but reduces runoff in the other three seasons. On the one hand, precipitation is concentrated in summer here, and mean monthly potential ET is lower than precipitation in July under most scenarios. The relatively small potential ET indicates that more precipitation may be transformed into lateral flow, instead of actual ET in summer. Therefore, the impact of LUCC on increased LATQ is more significant, which finally increases runoff in summer. On the other hand, the marked decrease in SURQ up to -11% in summer also indicates that more water may infiltrate in the soil due to increased forestland.

5.2. Impacts of model structure on this analysis

The analysis of the impact of LUCC on runoff reflects the model structure to some degree. In SWAT, the soil conservation service (SCS) curve number (CN) for moisture conditions of each land use type is different. Overall, the order of CN values for different land use types from high to low is agricultural land, grassland, and forestland. The higher value indicates more runoff to be generated (Zeng et al., 2017). The area weighted average of initial CN2 (i.e., the curve number under average moisture) over the study area is 57 and 55 under the 1970 and 2020 land use scenarios, respectively. The distribution of CN2 values for each HRUs under the 1970 and 2020 land use scenarios is shown in Fig. 13. Our study basin was divided into 19 subbasins, further generating 280 HRUs and 291 HRUs under the 1970 and 2020 land use scenarios, respectively. Subbasins (Nos. 10–19) are mainly distributed in the mountainous region and the increased forestland mainly occurs across these subbasins. Therefore, the CN2 value is generally higher in the right half part of Fig. 13(a) (Nos. 10–19) (i.e., the 1970 land use scenario) than that of Fig. 13(b) (i.e., the 2020 land use scenario).

Furthermore, more HRUs were generated under the 2020 land use scenario compared to those under the 1970 land use scenario. During the partition of HRUs in SWAT, the threshold level for land use was set to zero to ensure that the land use would not be influenced by the HRUs partition, meaning that no land use would be eliminated during the partition process. Therefore, different numbers of HRUs further reveal variations in land use distribution (i.e., the changed area and location of different land use types). Table 7 shows that most of the agricultural land will be transformed into forestland (673 km^2) and grassland (719 km^2) from 1970 to 2020, with most of the forestland transformed from grassland (1657 km^2). The increase in forestland is the main reason for the slightly decreased CN2 value. Based on the model mechanism, water yield of forestland is less than other land use types, which should result in less simulated streamflow under the 2020 land use scenario relative to that under the 1970 land use scenario. However, more factors, such as ET and infiltration can affect runoff generation, making interpretation of the results complicated.

Moreover, the partitioning of subbasins and HRUs in SWAT (e.g., the threshold level settings for land use, soil, and slope in the SWAT project determine the distribution of HRUs) would be different under different land use scenarios or basin outlets, affecting runoff generation. Nevertheless, the mechanism of runoff generation is complicated because of the synthesized effects of various land use types, complicated driving mechanisms, various human activities, as well as policy changes (Adhikari and Southworth, 2012; Wang et al., 2014; Wei et al., 2007). Future studies will focus on more reasonable prediction of LUCC and the mechanism of the impact of partitioning of subbasins and HRUs on runoff and hydrological processes.

5.3. Limitations of this study

This study is subjected to some limitations that need to be resolved in future work. First, the correction for spring flood is straightforward based on the logarithmic relationship between the total runoff in a year excluding the runoff in April and the ratio of it to the total runoff in a year. It would be more solid to account for the physical mechanism of the formation of spring flood associated with river thawing. Several factors, such as the date of the river freezing and thawing, and the channel discharge in the day when the river is frozen can be taken into account to improve the simulation of spring flood. Second, the prediction of the 2020 land use scenario is based on CA-Markov and mainly relies on the transition matrix from 2000 to 2010 land use maps. However, new land use management strategies may be implemented by the government during 2010–2020 that would change the 2020 land use and land cover scenario. In addition, the suitability maps for transition of different land use/land cover types are simplified, where only two constraints (i.e., slope and water body) are used to determine the suitable area of transformation from one land use type to others. Third, outputs of five GCMs under four RCPs were used to drive the SWAT model but the uncertainties have not been well examined. In addition, climate projections can be further corrected based on the local climate to better simulate the future runoff. Fourth, several simulated hydrological variables such as LATQ, GWQ, and PERC are difficult to examine due to the lack of observations. Therefore, the results are more of reflecting the model structure of SWAT.

6. Conclusion

The runoff of the Luanhe River basin in North China has decreased after the 1980s due to both climate (less precipitation) and human (soil and water conservation) factors. During recent years, afforestation projects have been greatly promoted, which has changed the land use/land cover in the basin and consequently affected the water availability. The increase in forestland but decrease in agricultural land and grassland influence the runoff generation. Based on the CA-Markov model, the land use scenario for 2020 is predicted, showing increases in forestland converted primarily from grassland and agricultural land relative to that in 1970 for the entire Luanhe River basin. Mean annual precipitation from five GCMs under four RCPs of the study area in the future (2020–2030) increases (1−7%) relative to the precipitation for the baseline period 1961–1979, and the seasonal precipitation will decrease only in winter.

SWAT, as one of the most widely used hydrological models that consider the effects of land use/cover on runoff, is set up in the upper reaches of the Luanhe River basin for the period 1961–1979, with the aim to simulate runoff for the period 2020–2030 under future climate change and two land use scenarios (i.e., 1970 and 2020), respectively. Results suggest that runoff in the future tends to increase, and the seasonal runoff only decreases in spring. Even though future precipitation

decreases in winter, the increased summer and fall precipitation may replenish soil moisture storage and increase runoff in winter. The relationship between the runoff depth and the RCPs is nonlinear, i.e., the maximum (57 mm) and minimum (50 mm) streamflow appears under the RCP4.5 and RCP6.0 scenarios, respectively, 39–58% higher than the observed runoff depth of 36 mm during the baseline period. The increased precipitation is the main driver for the increase in runoff. Furthermore, LUCC (afforestation) may lead to a slight decrease in mean annual runoff, and the seasonal runoff would increase in summer but decrease in the other three seasons for the study area. The climate change impact dominates changes in runoff over the study area.

Changes in ET, PERC, SURQ, GWQ, and LATQ under different land use scenarios indicate that the LUCC may lead to increases in ET and LATQ, but decreases in SURQ, PERC and GWQ for areas with limited changes in water bodies. Even though the surface runoff decreases, the lateral flow in summer contributes more water to the stream and therefore dominates the change in runoff. Furthermore, topography influences the impacts of LUCC on runoff generation to some degree.

Uncertainties in the future simulation exist because the LUCC prediction is based on the historical land use change. However, it may be influenced by future land use polices and human impacts that are difficult to predict. Future work can focus on improving prediction of LUCC, and evaluating uncertainties in climate projections as well as better interpreting the impacts of LUCC on runoff. Here we provide a solution to reveal changes in runoff by considering both LUCC and climate change. The results can be useful for water resource allocation and land use management in the Luanhe River basin, with important implications for afforestation and water diversion projects in China and globally under a changing environment.

Acknowledgements

Appendix A. Calculation of daily solar radiation and dew temperature

The solar radiation over the atmosphere was calculated by Eq. (1).

$$H_0 \frac{24}{\pi} I_{SC} E_0 \left[w T_{SR} \sin \delta \sin \phi + \cos \delta \cos \phi \sin(w T_{SR}) \right] \tag{1}$$

where H_0 is the radiation over the atmosphere (MJ/(m²·d)); I_{SC} is the solar constant (4.921 MJ/(m²Â·h)); E_0 is the correction factor of the eccentricity of the Earth orbit; w is the rotation angular velocity of the earth (0.2681 rad/h); T_{SR} is the length of daytime that the sun rises (h); δ is the solar declination (rad); and ϕ is the geographic latitude (rad).

E_0 is calculated by Eq. (2) proposed by Duffie et al. (1980).

$$E_0 = \left(\frac{r_0}{r} \right)^2 = 1 + 0.033 \cos \left(\frac{2\pi d_n}{365} \right) \tag{2}$$

where r_0 is the average distance of the sun from the earth (1AU); r is the distance between the sun and the earth on any day (AU); d_n is the order number of the day in the year from 1 to 365 (or 366). δ is calculated by equation (3) proposed by Perrin de Brichambaut (1975).

$$\delta = \sin^{-1} \left\{ 0.4 \sin \left[\frac{2\pi}{365} (d_n - 82) \right] \right\} \tag{3}$$

T_{SR} is calculated by Eq. (4):

$$T_{SR} = \frac{\cos^{-1}(-\tan \delta \tan \phi)}{w} \tag{4}$$

On cloudy days, the solar radiation cannot reach the ground directly and therefore a part of the radiation would loss when entering the atmosphere. The actual total solar radiation can be calculated by Eq. (5) (Pang et al., 2007).

$$H_L = 0.8 H_0 \tag{5}$$

where H_L is the total solar radiation on sunny day.

The daily solar radiation was calculated by empirical equation (6).

$$H = H_L (a + b \times S/S_L) \tag{6}$$

where H is the daily observed total solar radiation (MJ/(m²Â·d)); S is the sunshine duration; and S_L is the day length. Assuming that the solar elevation angle at sunrise and sunset is zero, S_L was calculated by Eq. (7) (Tong et al., 2005). a and b is empirical coefficients. Referring to the previous study (Guo, 2006a), the value of them was ascertained that $a = 0.21$ and $b = 0.86$.

$$S_L = \omega \times T_{SR} \times \frac{180}{\pi} \times \frac{2}{15} \tag{7}$$

The daily dew point temperature can be calculated by Eq. (8).

$$dew = \frac{[234.181 \log(e_a) - 184.2]}{[8.204 - \log(e_a)]} \tag{8}$$

where dew is the dew point temperature and e_a is the actual vapor pressure (mbar).

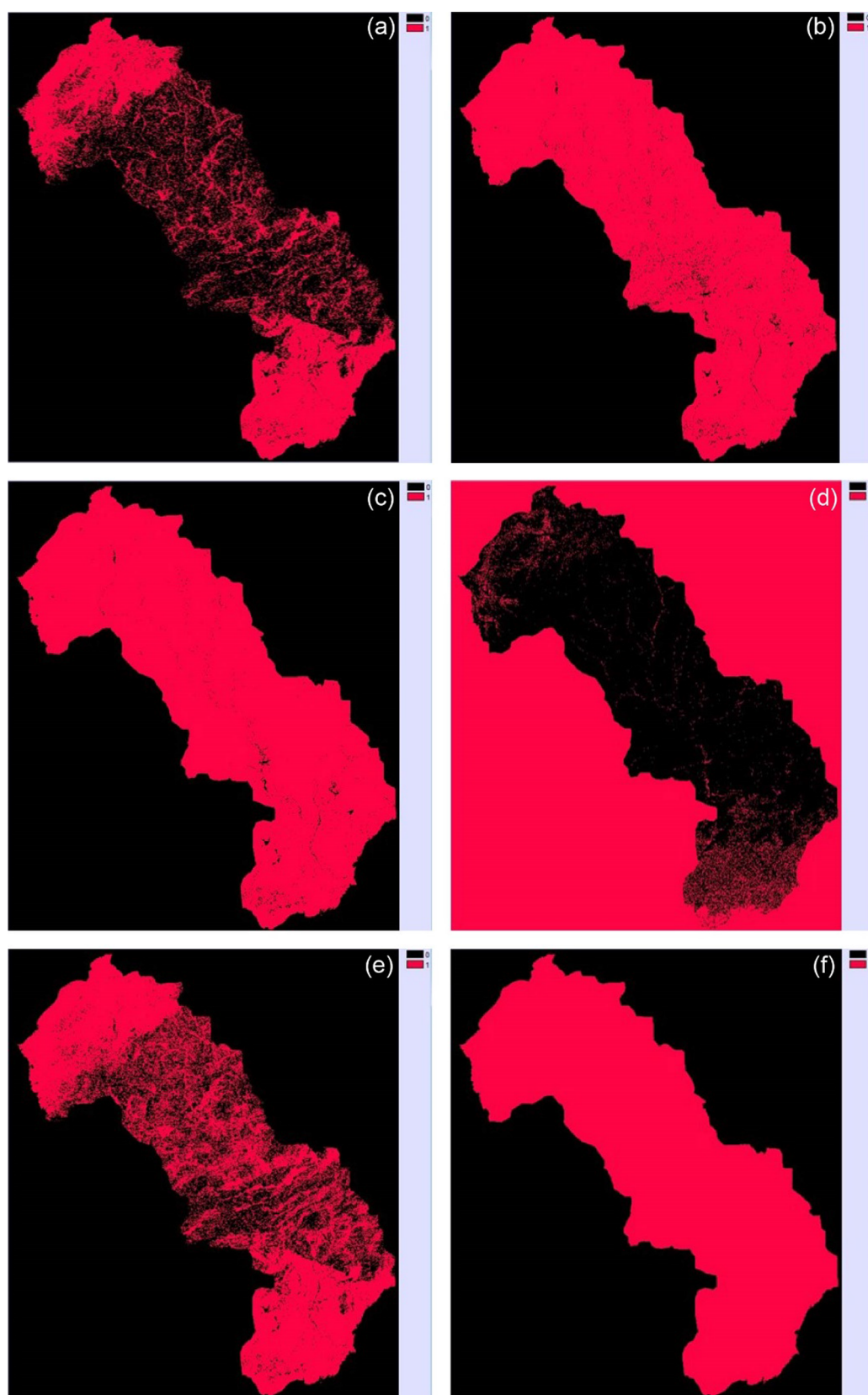**Appendix B. Suitability maps for different land uses/land covers.**

Fig. B1. Suitability maps for agriculture land (a), forestland (b), grassland (c), water (d), construction land (e) and unused land (f), with the suitable transformation area for each land use type coded with one (red color).

References

Aamery, N.A., Fox, J.F., Snyder, M., 2016. Evaluation of climate modeling factors impacting the variance of streamflow. J. Hydrol. 542, 125–142.

Abbaspour, K.C., et al., 2007. Modelling hydrology and water quality in the pre-alpine/alpine Thur watershed using SWAT. J. Hydrol. 333 (2–4), 413–430. https://doi.org/10.1016/j.jhydrol.2006.09.014.

Adhikari, S., Southworth, J., 2012. Simulating forest cover changes of bannerghatta national park based on a CA-markov model: a remote sensing approach. Remote Sens. 4 (12), 3215–3243. https://doi.org/10.3390/rs4103215.

Ahmadalipour, A., Moradkhani, H., Rana, A., 2017. Accounting for downscaling and model uncertainty in fine-resolution seasonal climate projections over the Columbia River Basin. Clim. Dyn. 1–17.

Baek, H.J., et al., 2013. Climate change in the 21st century simulated by HadGEM2-AO under representative concentration pathways. Asia-Pac. J. Atmos. Sci. 49 (5), 603–618. https://doi.org/10.1007/s13143-013-0053-7.

Baker, T.J., Miller, S.N., 2013. Using the Soil and Water Assessment Tool (SWAT) to assess land use impact on water resources in an East African watershed. J. Hydrol. 486, 100–111. https://doi.org/10.1016/j.jhydrol.2013.01.041.

Baldyga, T.J., Miller, S.N., Driese, K.L., Gichaba, C.M., 2008. Assessing land cover change in Kenya's Mau Forest region using remotely sensed data. Afr. J. Ecol. 46 (1), 46–54.

Basheer, A.K., Lu, H., Omer, A., Ali, A.B., Abdelgader, A.M.S., 2015. Impacts of climate change under CMIP5 RCP scenarios on the streamflow in the Dinder River and ecosystem habitats in Dinder National Park, Sudan. Hydrol. Earth Syst. Sci. Discuss. 12 (10), 10157–10195. https://doi.org/10.5194/hessd-12-10157-2015.

Becker, A., Mcdonnell, J.J., 1998. Topographical and ecological controls of runoff generation and lateral flows in mountain catchments.

Behera, M.D., Borate, S.N., Panda, S.N., Behera, P.R., Roy, P.S., 2012. Modelling and analyzing the watershed dynamics using Cellular Automata (CA)–Markov model – A geo-information based approach. J. Earth Syst. Sci. 121 (4), 1011–1024.

Bewket, W., Sterk, G., 2005. Dynamics in land cover and its effect on stream flow in the Chemoga watershed, Blue Nile basin. Ethiopia. Hydrol. Process. 19 (2), 445–458. https://doi.org/10.1002/hyp.5542.

Brown, A.E., Western, A.W., Mcmahon, T.A., Zhang, L., 2013. Impact of forest cover changes on annual streamflow and flow duration curves. J. Hydrol. 483 (3), 39–50.

Cao, Z., et al., 2010. Distribution and ecosystem risk assessment of polycyclic aromatic hydrocarbons in the Luan River, China. Ecotoxicology 19 (5), 827–837. https://doi.org/10.1007/s10646-010-0464-5.

Chen, L., Dong, Z., Fang, Q., Shan, C., 2013. Runoff changes in response to climate change and human activities scenarios of luanhe river basin. Water Resour. Power.

Chen, L., Frauenfeld, O.W., 2014. A comprehensive evaluation of precipitation simulations over China based on CMIP5 multimodel ensemble projections. J. Geophys. Res. Atmos. 119 (10), 5767–5786.

Chen, X., Xu, Y., Xu, C., Yao, Y., 2014. Assessment of precipitation simulations in China by CMIP5 multi-models. Adv. Clim. Change Res. 10 (3), 217–225.

Dars, G.H., 2013. Climate change impacts on precipitation extremes over the columbia river basin based on downscaled CMIP5 climate Scenarios. Dissert. Theses – Gradworks.

DeFries, R., Eshleman, K.N., 2004. Land-use change and hydrologic processes: a major focus for the future. Hydrol. Process. 18 (11), 2183–2186. https://doi.org/10.1002/hyp.5584.

Deng, H., Li, X., Chen, J., Zhang, M., Wan, H., 2003. Simulation of hydrological response to land cover changes in the suomo basin. Acta Geograph. Sin. 58 (1), 53–62.

Deng, X., Shi, Q., Zhang, Q., Shi, C., Yin, F., 2015. Impacts of land use and land cover changes on surface energy and water balance in the Heihe River Basin of China, 2000–2010. Phys. Chem. Earth Parts A/b/c 79–82, 2–10. https://doi.org/10.1016/j.pce.2015.01.002.

Dixon, B., Earls, J., 2012. Effects of urbanization on streamflow using SWAT with real and simulated meteorological data. Appl. Geogr. 35 (1–2), 174–190. https://doi.org/10.1016/j.apgeog.2012.06.010.

Du, J., Wang, G., Li, Y., 2015. Changes of land cover pattern in the source region of Yangtze River based on Markov process. Chin. J. Ecol. 34 (1), 195–203. https://doi.org/10.13292/j.1000-4890.2015.0029.

Duffie, J.A., Beckman, W.A., Mcgowan, J., 1980. Solar Engineering of Thermal Processes. Wiley, pp. pp.

Eisner, S., et al., 2017. An ensemble analysis of climate change impacts on streamflow seasonality across 11 large river basins. Clim. Change 141 (3), 1–17.

Eum, H.I., Dibike, Y., Prowse, T., 2016. Climate-induced alteration of hydrologic indicators in the athabasca river basin, Alberta, Canada. J. Hydrol. 544.

Gao, L., Xu, J., 2010. Prediction of land use in anning city based on markov model. Yunnan Geograp. Environ. Res. 22 (2).

Gashaw, T., Tulu, T., Argaw, M., Worqlul, A.W., 2017. Evaluation and prediction of land use/land cover changes in the Andassa watershed, Blue Nile Basin, Ethiopia. Environ. Syst. Res. 6 (1), 17.

Guo, B., 2006a. Zoning model analysis on the relation between global solar radiation and sunshine hours. Xi'an University of Architecture and Technology.

Guo, D., 2006b. Prediction of land use and land cover patterns in recent Yellow River Delta using Markov Chain model. Soils 38 (1), 42–47.

Gupta, S.C., Kessler, A.C., Brown, M.K., Zvomuya, F., 2015. Climate and agricultural land use change impacts on streamflow in the upper midwestern United States. Water Resour. Res. 51 (7), 5301–5317.

Halmy, M.W.A., Gessler, P.E., Hicke, J.A., Salem, B.B., 2015. Land use/land cover change detection and prediction in the north-western coastal desert of Egypt using Markov-CA. Appl. Geogr. 63, 101–112. https://doi.org/10.1016/j.apgeog.2015.06.015.

He, B., Gao, M., Zhao, J., 2014. Dynamic changes of land cover based on Markov model in

Turpan City. Res. Soil Water Conserv. 21 (5), 41–48. https://doi.org/10.13869/j.cnki.rswc.2014.05.008.

Hempel, S., Frieler, K., Warszawski, L., Schewe, J., Piontek, F., 2013. A trend-preserving bias correction – The ISI-MIP approach. Earth Syst. Dynam. 4 (2), 219–236.

Hoang, L., et al., 2017. Predicting saturation-excess runoff distribution with a lumped hillslope model SWAT-HS. Hydrol. Processes. 31.

Houston, J., 2006. Variability of precipitation in the Atacama Desert: its causes and hydrological impact. Int. J. Climatol. 26 (15), 2181–2198. https://doi.org/10.1002/joc.1359.

Iacono, M., Levinson, D., El-Geneidy, A.M., Rania, W., 2012. A markov chain model of land use change in the twin cities. J. Land Use Mobil. Environ. 8 (3), 1–24. https://doi.org/10.6092/1970-9870/2985.

Kallali, H., Anane, M., Jellali, S., Tarhouni, J., 2007. GIS-based multi-criteria analysis for potential wastewater aquifer recharge sites. Desalination 215 (1), 111–119.

Kamga, F.M., 2001. Impact of greenhouse gas induced climate change on the runoff of the Upper Benue River (Cameroon). J. Hydrol. 252 (1), 145–156.

Kathumo, V.M. et al., 2011. Effects of land-use and climate changes on hydrological processes in the River Gucha catchment, Kenya, Natural Resources Management and Land Use. Proceedings of the Cluster Workshop, Nairobi, Kenya, 30th November - 2nd December 2011.

Lambin, E.F., Meyfroidt, P., 2011. Global land use change, economic globalization, and the looming land scarcity. Proc. Natl. Acad. Sci. U.S.A. 108 (9), 3465–3472. https://doi.org/10.1073/pnas.1100480108.

Leng, G., Tang, Q., Rayburg, S., 2015. Climate change impacts on meteorological, agricultural and hydrological droughts in China. Global Planet. Change 126 (126), 23–34.

Li, F., 2008. The theory of SWAT model and its applicaion. China Rural Water Hydropower 3, 24–27.

Li, J., 2005. Study on the Distributed Rainfall-Runoff Modelling of Luanhe Watershed. Tianjin University.

Li, J., Tan, S., Chen, F., Feng, P., 2014. Quantitatively analyze the impact of land use/land cover change on annual runoff decrease. Nat. Hazards 74 (2), 1191–1207. https://doi.org/10.1007/s11069-014-1237-x.

Li, L., Jiang, D., Li, J., Liang, L., Zhang, L., 2007. Advances in hydrological response to land use /land cover change. J. Natural Resour. 22 (2), 211–224.

Li, L., Jiang, D., Yang, J., Li, J., 2010. Study on hydrological response to land use and land cover change in Dali River Basin, Shaanxi Province. Geograph. Res. 29 (7), 1233–1243.

Li, W., Zhang, H., Li, J., Pang, C., Wang, X., 2017. Write the Green Legend in the Earth of Yanzhao. DAILY, HEBEI.

Li, Y., Huang, S., 2015. Landscape Ecological Risk Responses to Land Use Change in the Luanhe River Basin, China. Sustainability 7 (12), 16631–16652. https://doi.org/10.3390/su71215835.

Liang, W., et al., 2015. Quantifying the impacts of climate change and ecological restoration on streamflow changes based on a Budyko hydrological model in China's Loess Plateau. Water Resour. Res. 51 (8), 6500–6519.

Liu, C., Dong, Z., Fang, Q., Shan, C., 2013. Runoff change in response to climate change and human activities scenarios of luanhe river basin. Water Resour. Power 31 (9), 12–15.

Liu, Y., 2012. An analysis of the hydrology, geology and economic situation of Luanhe River basin. J. Hebei Normal Univers. National. 32 (2), 24–26.

Ma, J., et al., 2010. Characteristics of climate resources under global climate change in the North China Plain. Acta Ecol. Sin. 30 (14), 3818–3827.

Middelkoop, H., et al., 2001. Impact of climate change on hydrological regimes and water resources management in the Rhine basin. Clim. Change 49 (1–2), 105–128.

Moulin, L., Gaume, E., Obled, C., 2008. Uncertainties on mean areal precipitation: assessment and impact on streamflow simulations. Hydrol. Earth Syst. Sci. Discuss. 5 (4), 2067–2110. https://doi.org/10.5194/hessd-5-2067-2008.

Muller, M.R., Middleton, J., 1994. A Markov model of land-use change dynamics in the Niagara Region, Ontario Canada. Landsc. Ecol. 9 (2), 151–157. https://doi.org/10.1007/bf00124382.

Najafi, M.R., Moradkhani, H., 2015. A hierarchical Bayesian approach for the analysis of climate change impact on runoff extremes. Hydrol. Process. 28 (26), 6292–6308.

Neupane, R.P., White, J.D., Alexander, S.E., 2015. Projected hydrologic changes in monsoon-dominated Himalaya Mountain basins with changing climate and deforestation. J. Hydrol. 525, 216–230.

Ouyang, F., et al., 2015. Impacts of climate change under CMIP5 RCP scenarios on streamflow in the Huangnizhuang catchment. Stoch. Env. Res. Risk Assess. 29 (7), 1781–1795. https://doi.org/10.1007/s00477-014-1018-9.

Pang, J., Xu, Z., Liu, C., 2007. Weather generator and database in the SWAT model. J. China Hydrol. 27 (5).

Perrin de Brichambaut, C.C.A.F.E.D.E.S., 1975. supplement au no.1 Editions, Paris.

Pervez, M.S., Henebry, G.M., 2015. Assessing the impacts of climate and land use and land cover change on the freshwater availability in the Brahmaputra River basin ✩. J. Hydrol.: Reg. Stud. 3, 285–311.

RL Wilby, S.C., 2004. Guidelines for use of climate scenarios developed from statistical downscaling method.

Saifullah, M., Li, Zhijia, Li, Qiaoling, Zaman, Muhammad, Hashim, Sarfraz, 2016. Quantitative estimation of the impact of precipitation and land surface change on hydrological processes through statistical modeling. Adv. Meteorol. 2016, 1–15. https://doi.org/10.1155/2016/6130179.

Sang, L., Zhang, C., Yang, J., Zhu, D., Yun, W., 2011. Simulation of land use spatial pattern of towns and villages based on CA–Markov model. Math. Comput. Modell. 54 (3–4), 938–943. https://doi.org/10.1016/j.mcm.2010.11.019.

Savenije, H.H.G., 2010. Topography driven conceptual modelling (FLEX-Topo). Hydrol. Earth Syst. Sci. 7 (4), 4635–4656.

Shan, C., Dong, Z., Fu, X., Fang, Q., Liu, C., Liu, Q., 2013. Rules of Runoff Variation in Luanhe River basin in recent 50 years. S. N. Water Trans. Water Sci. Technol. 11 (4), 5–8.

Shawul, A.A., Alamirew, T., Dinka, M.O., 2013. Calibration and validation of SWAT model and estimation of water balance components of Shaya mountainous watershed, Southeastern Ethiopia. Hydrol. Earth Syst. Sci. Discuss. 10 (11), 13955–13978.

Shen, Y., Xiong, A., 2016. Validation and comparison of a new gauge-based precipitation analysis over mainland China. Int. J. Climatol. 36 (1), 252–265. https://doi.org/10.1002/joc.4341.

Shi, P., Li, W., 2001. Influence of forest cover change on hydrological process and watershed runoff. J. Natur. Resour. 16.

Shi, X., 2013. Study on distributed hydrological simulation and drought evaluation method in Luanhe River basin based on SWAT model, Northeast Institute of Geography and Agroecology, Chinese Academy of Sciences.

Shi, X., Yang, Z., Yan, D., Li, Y., Yuan, Z., 2014. On hydrological response to land-use/cover change in Luanhe River basin. Adv. Water Sci. 25 (1), 21–27.

Singh, S.K., Mustak, S., Srivastava, P.K., Szabó, S., Islam, T., 2015. Predicting spatial and decadal LULC changes through cellular automata markov chain models using earth observation datasets and geo-information. Environ. Process. 2 (1), 61–78.

Siriwardena, L., Finlayson, B.L., Mcmahon, T.A., 2006. The impact of land use change on catchment hydrology in large catchments: The Comet River, Central Queensland, Australia. J. Hydrol. 326 (1–4), 199–214.

Subedi, P., Subedi, K., Thapa, B., 2013. Application of a hybrid cellular automaton – Markov (CA-Markov) model in land-use change prediction: a case study of saddle creek drainage basin, Florida. Sci. Educ. 1 (6), 126–132.

Sun, Q., Miao, C., Duan, Q., 2016. Extreme climate events and agricultural climate indices in China: CMIP5 model evaluation and projections. Int. J. Climatol. 36 (1), 43–61.

Teklesadik, A.D., et al., 2017. Inter-model comparison of hydrological impacts of climate change on the Upper Blue Nile basin using ensemble of hydrological models and global climate models. Clim. Change 1–16.

Teshager, A.D., Gassman, P.W., Secchi, S., Schoof, J.T., Misgna, G., 2016. Modeling agricultural watersheds with the soil and water assessment tool (SWAT): calibration and validation with a novel procedure for spatially explicit HRUs. Environ. Manage.

57 (4), 894–911. https://doi.org/10.1007/s00267-015-0636-4.

Thampi, S.G., Raneesh, K.Y., Surya, T.V., 2010. Influence of scale on SWAT model calibration for streamflow in a river basin in the humid tropics. Water Resour. Manage. 24 (15), 4567–4578.

Tong, C., Zhang, W., Tang, Y., Wang, H., 2005. Estimation of daily solar radiation in China. Agric. Meteorol.

Wang, S., Kang, S., Zhang, L., Li, F., 2008. Modelling hydrological response to different land-use and climate change scenarios in the Zamu River basin of northwest China. Hydrol. Process. 22 (14), 2502–2510.

Wang, Z., Li, C., Yu, F., Xu, Z., Zhao, N., 2014. Research progress on the impacts of land use/cover change on runoff. S. N. Water Trans. Water Sci. Technol. 12 (1), 88–93.

Weedon, G.P., et al., 2011. Creation of the WATCH forcing data and its use to assess global and regional reference crop evaporation over land during the twentieth century. J. Hydrometeorol. 12 (5), 823–848.

Wei, W., et al., 2007. The effect of land uses and rainfall regimes on runoff and soil erosion in the semi-arid loess hilly area, China. J. Hydrol. 335 (3–4), 247–258. https://doi.org/10.1016/j.jhydrol.2006.11.016.

Wilby, R.L., Hay, L.E., Leavesley, G.H., 1999. A comparison of downscaled and raw GCM output: implications for climate change scenarios in the San Juan River basin, Colorado. J. Hydrol. 225 (1–2), 67–91. https://doi.org/10.1016/s0022-1694(99)00136-5.

Yu, F., Shi, Z., Li, B., Yang, J., Peng, H., 2008. The SWAT model and its application. Technol. Soil Water Conserv. 5, 1–4.

Yu, W., Zang, S., Wu, C., Liu, W., Na, X., 2011. Analyzing and modeling land use land cover change (LUCC) in the Daqing City China. Appl. Geogr. 31 (2), 600–608.

Zeng, Z., Tang, G., Hong, Y., Zeng, C., Yang, Y., 2017. Development of an NRCS curve number global dataset using the latest geospatial remote sensing data for worldwide hydrologic applications. Remote Sens. Lett. 8 (6), 528–536.

Zhang, M., Wei, X., 2012. The cumulative effects of forest disturbance on streamflow in a large watershed in the central interior of British Columbia, Canada. Hydrol. Earth Syst. Sci. Discuss. 9 (3), 2855–2895.

Zhang, Y., et al., 2014. Impacts of climate change and land use change on runoff of forest catchment in northeast China. Hydrol. Process. 28 (2), 186–196. https://doi.org/10.1002/hyp.9564.